

On the discretization and application of two space-time boundary integral equations for 3D wave propagation problems in unbounded domains

*Original*

On the discretization and application of two space-time boundary integral equations for 3D wave propagation problems in unbounded domains / Falletta, Silvia; Monegato, Giovanni; Scuderi, Letizia. - In: APPLIED NUMERICAL MATHEMATICS. - ISSN 0168-9274. - STAMPA. - 124:(2018), pp. 22-43. [10.1016/j.apnum.2017.10.001]

*Availability:*

This version is available at: 11583/2684413 since: 2019-09-04T12:16:38Z

*Publisher:*

Elsevier

*Published*

DOI:10.1016/j.apnum.2017.10.001

*Terms of use:*

This article is made available under terms and conditions as specified in the corresponding bibliographic description in the repository

*Publisher copyright*

Elsevier postprint/Author's Accepted Manuscript

© 2018. This manuscript version is made available under the CC-BY-NC-ND 4.0 license  
<http://creativecommons.org/licenses/by-nc-nd/4.0/>. The final authenticated version is available online at:  
<http://dx.doi.org/10.1016/j.apnum.2017.10.001>

(Article begins on next page)

# On the discretization and application of two space-time boundary integral equations for 3D wave propagation problems in unbounded domains<sup>\*</sup>

S. Falletta<sup>a</sup>, G. Monegato<sup>b</sup>, L. Scuderi<sup>c</sup>

*Dipartimento di Scienze Matematiche, Politecnico di Torino, Italy.*

*Email: <sup>a</sup>silvia.falletta@polito.it, <sup>b</sup>giovanni.monegato@polito.it, <sup>c</sup>letizia.scuderi@polito.it*

---

## Abstract

In this paper, we consider 3D wave propagation problems in unbounded domains, such as those of acoustic waves in non viscous fluids, or of seismic waves in (infinite) homogeneous isotropic materials, where the propagation velocity  $c$  is much higher than 1. For example, in the case of air and water  $c \approx 343 \text{ m/s}$  and  $c \approx 1500 \text{ m/s}$  respectively, while for seismic P-waves in linear solids we may have  $c \approx 6000 \text{ m/s}$  or higher. These waves can be generated by sources, possible away from the obstacles. We further assume that the dimensions of the obstacles are much smaller than that of the wave velocity, and that the problem transients are not excessively short.

For their solution we consider two different approaches. The first directly uses a known space-time boundary integral equation to determine the problem solution. In the second one, after having defined an artificial boundary delimiting the region of computational interest, the above mentioned integral equation is interpreted as a non reflecting boundary condition to be coupled with a classical finite element method.

For such problems, we show that in some cases the computational cost and storage, required by the above numerical approaches, can be significantly reduced by taking into account a property that till now has not been considered. To show the effectiveness of this reduction, the proposed approach is applied to several problems, including multiple scattering.

*Key words:* exterior wave propagation problems; space-time boundary integral equations; non reflecting boundary conditions; numerical methods

---

<sup>\*</sup> This work was supported by the Ministero dell'Istruzione, dell'Università e della Ricerca of Italy, under the research program PRIN 2012: Innovative methodologies for PDE-based numerical modelling, and by the GNCS-INDAM 2016 research program: Accoppiamento FEM-BEM non conforme mediante tecniche di decomposizione di dominio di tipo mortar.

## 1. Introduction

In the last decades, space-time Boundary Integral Equations (BIE) have been successfully applied to wave propagation problems defined in the exterior of a bounded domain (see, for example, [9],[24],[3],[19],[26],[15],[10],[2],[27],[16],[5], [4],[25],[18],[17],[22],[12]).

Most of them, however, are for homogeneous problems with trivial initial values. Furthermore, they are generally used to determine the problem solution at chosen points. Only in the last few years (see [13], [2], [14],[6]), a BIE for the classical wave equation has been used to define a Non Reflecting Boundary Condition (NRBC) on a chosen artificial boundary, surrounding the computational domain. Its discretization is then coupled with that of the domain of interest by means of finite elements or finite differences.

In the case of the classical 3D non homogeneous wave equation, the problem we consider in this paper is the following:

$$\begin{cases} \frac{1}{c^2}u_{tt}^e(\mathbf{x}, t) - \Delta u^e(\mathbf{x}, t) &= f(\mathbf{x}, t) & \text{in } \Omega^e \times (0, T) \\ u^e(\mathbf{x}, t) &= g(\mathbf{x}, t) & \text{in } \Gamma \times (0, T) \\ u^e(\mathbf{x}, 0) &= u_0(\mathbf{x}) & \text{in } \Omega^e \\ u_t^e(\mathbf{x}, 0) &= v_0(\mathbf{x}) & \text{in } \Omega^e \end{cases} \quad (1)$$

where  $\Omega^e = \mathbb{R}^3 \setminus \overline{\Omega^i}$ ,  $\Omega^i$  being a bounded open domain, having a smooth boundary  $\Gamma$ , or the union  $\cup_{k=1}^{\kappa} \Omega_k^i$  of well separated domains of this type. As often occurs in practical situations, we assume that the initial values  $u_0$ ,  $v_0$  and the source term  $f$  have local supports. Furthermore, we also assume that these data satisfy the smoothness and compatibility conditions which guarantee a sufficiently smooth solution  $u^e$ , as required (see [15],[24]) by the numerical approach we will describe in the next section.

To solve problem (1) we will consider the following single-double layer BIE (see [14]):

$$\frac{1}{2}u^e(\mathbf{x}, t) - (\mathbf{V}\partial_{\mathbf{n}}u^e)(\mathbf{x}, t) + (\mathbf{K}u^e)(\mathbf{x}, t) = I_{u_0}(\mathbf{x}, t) + I_{v_0}(\mathbf{x}, t) + I_f(\mathbf{x}, t) \quad \mathbf{x} \in \Gamma, \quad (2)$$

with

$$\mathbf{V}\psi(\mathbf{x}, t) := \int_0^t \int_{\Gamma} G(\mathbf{x} - \mathbf{y}, t - \tau) \psi(\mathbf{y}, \tau) d\Gamma_{\mathbf{y}} d\tau = \int_{\Gamma} \frac{\psi(\mathbf{y}, t - \|\mathbf{x} - \mathbf{y}\|/c)}{4\pi\|\mathbf{x} - \mathbf{y}\|} d\Gamma_{\mathbf{y}} \quad (3)$$

and

$$\mathbf{K}\varphi(\mathbf{x}, t) := \int_0^t \int_{\Gamma} \partial_{\mathbf{n}}G(\mathbf{x} - \mathbf{y}, t - \tau) \varphi(\mathbf{y}, \tau) d\Gamma_{\mathbf{y}} d\tau = \int_{\Gamma} \partial_{\mathbf{n}} \frac{\varphi(\mathbf{y}, t - \|\mathbf{x} - \mathbf{y}\|/c)}{4\pi\|\mathbf{x} - \mathbf{y}\|} d\Gamma_{\mathbf{y}}. \quad (4)$$

The last expressions in (3) and (4) have been obtained by interchanging (see [15]) the time and space integrals in the corresponding representations, and using the wave equation fundamental solution expression

$$G(\mathbf{x}, t) = \frac{\delta(t - \|\mathbf{x}\|/c)}{4\pi\|\mathbf{x}\|}, \quad (5)$$

where  $\delta(\cdot)$  is the well known Dirac delta function. The symbol  $\partial_{\mathbf{n}} = \partial_{\mathbf{n}_{\mathbf{y}}}$  denotes the outward unit normal (distributional) derivative, with respect to the  $\mathbf{y}$ -variable, on the boundary  $\Gamma$ .

The “volume” terms  $I_{u_0}$ ,  $I_{v_0}$  and  $I_f$  are generated by the non homogeneous initial conditions and the non trivial source, respectively. These volume terms have the following integral representations (see [15]):

$$I_{u_0}(\mathbf{x}, t) = \frac{\partial}{\partial t} \int_{\text{supp}(u_0)} G(\mathbf{x} - \mathbf{y}, t) u_0(\mathbf{y}) d\mathbf{y}, \quad (6)$$

$$I_{v_0}(\mathbf{x}, t) = \int_{\text{supp}(v_0)} G(\mathbf{x} - \mathbf{y}, t) v_0(\mathbf{y}) d\mathbf{y}, \quad (7)$$

$$I_f(\mathbf{x}, t) = \int_0^t \int_{\text{supp}(f)} G(\mathbf{x} - \mathbf{y}, t - \tau) f(\mathbf{y}, \tau) d\mathbf{y} d\tau. \quad (8)$$

The mapping properties of the above operators  $\mathbf{V}$ ,  $\mathbf{K}$ , when these are acting in proper functional spaces, are well-known; see, for example, [24], [21], [28]. In particular, for any real  $r \geq 0$ ,

$$\mathbf{V} : H_0^{r+1}(0, T; H^{-1/2}(\Gamma)) \rightarrow H_0^r(0, T; H^{1/2}(\Gamma)) \quad (9)$$

and

$$\mathbf{K} : H_0^{r+3/2}(0, T; H^{1/2}(\Gamma)) \rightarrow H_0^r(0, T; H^{1/2}(\Gamma)) \quad (10)$$

are bounded.

The above spaces are defined as follows. Set first  $H_0^r(0, T) = \{g|_{(0, T)} : g \in H^r(\mathbb{R}) \text{ with } g \equiv 0 \text{ on } (-\infty, 0)\}$ , where  $H^r$  denotes the classical Sobolev space of order  $r$ . When  $r$  is an integer, this space consists of those functions  $g$  whose  $r$ -th distributional derivative is in  $L^2(0, T)$  and which have  $g(0) = \dots g^{(r-1)}(0) = 0$ . Then:

- $H_0^r(0, T; X)$  is the space of  $H_0^r(0, T)$  functions of  $t$ ,  $\phi(\mathbf{x}, t)$ , such that, setting  $\phi(\mathbf{x}, t) = \phi(t)(\mathbf{x})$ , we have  $\phi(t) \in X$ , with  $\|\phi(t)\|_X \|_{H^r(0, T)} < \infty$ .
- $H^{1/2}(\Gamma)$  and  $H^{-1/2}(\Gamma)$  are the trace space on the boundary  $\Gamma$ , of  $H^1(\Omega^e)$  functions, and the corresponding dual space, respectively.

Recalling the well known embedding property:  $H^r(0, T) \subset C^m[0, T]$  for  $r > m + 1/2$ , from (9) and (10) we deduce that for  $r > 3/2$  we have

$$\mathbf{V} : H_0^r(0, T; H^{-1/2}(\Gamma)) \rightarrow C([0, T]; H^{1/2}(\Gamma)),$$

while if  $r > 2$ ,

$$\mathbf{K} : H_0^r(0, T; H^{1/2}(\Gamma)) \rightarrow C([0, T]; H^{1/2}(\Gamma)).$$

Moreover, under the assumptions we have made on the problem data, all terms of the above BIE will be, in particular, continuous functions of  $\mathbf{x} \in \Gamma$ .

Once the function  $\lambda = \partial_{\mathbf{n}} u^e$  has been determined, the solution  $u^e$ , for  $\mathbf{x} \in \Omega^e$  and  $t \in [0, T]$ , is given by the following integral representation:

$$u^e(\mathbf{x}, t) = \int_0^t \int_{\Gamma} G(\mathbf{x} - \mathbf{y}, t - \tau) \lambda(\mathbf{y}, \tau) d\Gamma_{\mathbf{y}} d\tau - \int_0^t \int_{\Gamma} \partial_{\mathbf{n}} G(\mathbf{x} - \mathbf{y}, t - \tau) g(\mathbf{y}, \tau) d\Gamma_{\mathbf{y}} d\tau + I(\mathbf{x}, t), \quad (11)$$

where we have set  $I(\mathbf{x}, t) = I_{u_0}(\mathbf{x}, t) + I_{v_0}(\mathbf{x}, t) + I_f(\mathbf{x}, t)$ .

We also recall that if we consider the interior problem associated with (1), whose solution is denoted by  $u^i(\mathbf{x}, t)$ , hence define the normal derivative jump across  $\Gamma$ :  $\varphi(\mathbf{y}, \tau) = \partial_n u^e(\mathbf{y}, \tau) - \partial_n u^i(\mathbf{y}, \tau)$ , the following single-layer BIE (see [24] and [15]) holds:

$$\int_0^t \int_{\Gamma} G(\mathbf{x} - \mathbf{y}, t - \tau) \varphi(\mathbf{y}, \tau) d\Gamma_{\mathbf{y}} d\tau = g(\mathbf{x}, t) - I(\mathbf{x}, t), \quad \mathbf{x} \in \Gamma, \quad t \in [0, T]. \quad (12)$$

Once the function  $\varphi$  has been determined, the solution  $u^e$  is given by the following integral representation:

$$u^e(\mathbf{x}, t) = \int_0^t \int_{\Gamma} G(\mathbf{x} - \mathbf{y}, t - \tau) \varphi(\mathbf{y}, \tau) d\Gamma_{\mathbf{y}} d\tau + I(\mathbf{x}, t), \quad \mathbf{x} \in \Omega^e, \quad t \in [0, T]. \quad (13)$$

Actually, if one has to compute the solution  $u^e(\mathbf{x}, t)$  only in a small region away from the domain  $\Omega^i$ , the best approach is the Boundary Element Method (BEM) defined by representations (12) and (13).

In the following, for notational simplicity, we drop the superscript “e” from  $u^e$  and set  $\lambda(\mathbf{y}, t) = \partial_n u(\mathbf{y}, t)$ .

Very recently, in [14] (see also [6]), for the solution of (1), we have proposed to use (2) as a global Non Reflecting Boundary Condition, to be imposed on a chosen artificial boundary  $\mathcal{B}$  delimiting the domain of interest  $\Omega$ . This NRBC is interpreted as a relationship that the problem solution and its normal derivative must satisfy on  $\mathcal{B}$ , to avoid spurious wave reflections. It is of exact type and it holds for a (smooth) surface of arbitrary shape; therefore, it can be used also in situations of multiple scattering, and even in more general ones. Moreover, it allows the problem to have non trivial data, whose (local) supports do not have necessarily to be included in the  $\Omega$  domain, as it is usually done, in particular when they are away from the domain of interest. In such a case, the proposed NRBC naturally includes the effects of these data and it is automatically transparent for outgoing waves as well as for incoming ones.

For the discretization of the BIE (2), or of the corresponding NRBC, namely for the approximation of the single and double layer operators, we have proposed a numerical scheme which is based on a second order Lubich discrete convolution quadrature formula (see [23]), later denoted by the symbol BDF2, for the discretization of the time integral, coupled with a classical collocation method in space. The BDF2 formula is obtained from the classical second order Backward Differentiation Formula for ordinary differential equations. Its computational complexity is of order  $N \log N$ , being  $N$  the total number of time steps performed, while that of the global (space-time) discretization is of order  $M^2 N \log N$ , where  $M$  is the number of collocation points chosen on the domain surface. The required working storage is  $M^2 N$ . We recall that, in the case of the NRBC, when the discretization of the bounded domain  $\Omega$  where we apply the chosen finite element scheme is refined, and the time step-size is simultaneously reduced, the accuracy of the NRBC discretization increases.

In all the papers where the above approach has been applied, the wave propagation velocity has been taken equal to 1, and also the size of the physical domains is of order 1. Furthermore, the final time instant  $T$  is generally not large, let us say, from 1 up to about 50. Of course, by properly scaling the variables, we can always reduce problem (1) to an

equivalent one having unitary velocity and diameter. For example, in the case of velocity  $c$  and domain diameter  $d$ , it is sufficient to set  $\mathbf{x} = d\bar{\mathbf{x}}$  and  $t = \frac{d}{c}\bar{t}$ . This scaling, however, changes also the original time interval of integration  $(0, T]$  into  $(0, \bar{T}]$ , with  $\bar{T} = cT/d$ , and in several applications  $T$  is not small. This is the case, for example, we have when the source  $f$  is far away from the domain  $\Omega^i$ , or when we have to deal with wave packets, or multiple scattering - multiple sources problems, or scattering from (non convex) domains having cavities. That is, when we have to solve wave propagation problems having a long transient phase with respect to  $d/c$ . Thus, in these cases, when  $c$  is much larger than  $d$ ,  $\bar{T}$  can be much larger than 50. These are the situations that we examine in this paper. To show explicitly the dependence on the physical parameters of the conditions we will derive in Section 2, we will not take advantage of the above mentioned changes of variables.

In particular, we consider 3D wave propagation problems in unbounded domains, such as those of acoustic waves in non viscous fluids, of seismic waves in (infinite) homogeneous isotropic materials, or of electromagnetic waves, where the propagation velocity  $c$  is much higher than 1. For example, for the acoustic waves in air and water we have  $c \approx 343 \text{ m/s}$  and  $c \approx 1500 \text{ m/s}$ , respectively, while for seismic P-waves in linear solids we may have  $c \approx 6000 \text{ m/s}$  or higher. We allow waves generated by sources, that can be located far away from the obstacles. Finally, we assume that the order of magnitude of the obstacles is much smaller than that of the wave velocity, and that the problem transients are not excessively short.

Our main goal is to show that for such problems, the computational cost and storage required by the numerical approach mentioned above can be significantly reduced by taking into account a property that, to our best knowledge, till now has been ignored or underestimated. This allows to replace, in the above mentioned computational cost and working storage, the integer  $N$  by a much smaller (positive) integer  $N_0$ , explicitly defined by a simple formula.

We note that in some papers (see [20], [19], [5], [17]), to reduce the method computational cost and storage, a rule for approximating the matrices generated by the chosen Lubich discrete convolution, when this is combined with a Galerkin space discretization, by corresponding sparse ones have been proposed and examined when  $c = 1$ ,  $d \approx 1$ . However, this is valid only for the single-layer BIE representation, not for the single-double BIE case we consider in this paper. Moreover, as it is pointed out in Remark 3.6 of this paper, this rule turns out to be little effective when it is applied to the problems we consider in this paper.

Thus, after briefly recalling, in Section 2, definitions and construction of the BIE discretization, in Section 3 we derive some bounds for the coefficients of the (time) discrete convolution quadrature, when the wave propagation velocity is much higher than the obstacle dimensions. These bounds will show how computational cost and work storage can be significantly reduced. Then, in Section 4, we apply the proposed numerical approach to several problems; these include cases where the BIE plays the role of a NRBC and a multiple scattering example.

## 2. Discretization of the single-double layer BIE

In this section we outline the formulas used in [14] to discretize the BIE formulation (2).

### 2.1. Approximation in time

The single and double layer operators appearing in (2) are approximated by combining the second order BDF2 convolution quadrature formula of Lubich (see [23]) with a classical space collocation method. Thus, the interval  $[0, T]$  is subdivided into  $N$  steps of equal length  $\Delta_t = T/N$  and the BIE is collocated at the discrete time levels  $t_n = n\Delta_t$ ,  $n = 0, \dots, N$ :

$$\frac{1}{2}u(\mathbf{x}, t_n) - (\mathbf{V}\lambda)(\mathbf{x}, t_n) + (\mathbf{K}u)(\mathbf{x}, t_n) = I_{u_0}(\mathbf{x}, t_n) + I_{v_0}(\mathbf{x}, t_n) + I_f(\mathbf{x}, t_n). \quad (14)$$

The time integrals appearing in the definition of the single and double layer operators (see (3), (4)) are discretized by means of the above mentioned second order Lubich convolution quadrature formula (see [14]). We obtain:

$$\begin{aligned} (\mathbf{V}\lambda)(\mathbf{x}, t_n) &\approx \sum_{j=0}^n \int_{\Gamma} \omega_{n-j}^{\mathbf{V}} \left( \Delta_t; \frac{\|\mathbf{x} - \mathbf{y}\|}{c} \right) \lambda(\mathbf{y}, t_j) d\Gamma_{\mathbf{y}}, \quad n = 0, \dots, N, \\ (\mathbf{K}u)(\mathbf{x}, t_n) &\approx \sum_{j=0}^n \int_{\Gamma} \omega_{n-j}^{\mathbf{K}} \left( \Delta_t; \frac{\|\mathbf{x} - \mathbf{y}\|}{c} \right) u(\mathbf{y}, t_j) d\Gamma_{\mathbf{y}}, \quad n = 0, \dots, N, \end{aligned} \quad (15)$$

whose coefficients  $\omega_n^{\mathcal{J}}$ ,  $\mathcal{J} = \mathbf{V}, \mathbf{K}$ , are given by

$$\omega_n^{\mathcal{J}} \left( \Delta_t; \frac{\|\mathbf{x} - \mathbf{y}\|}{c} \right) = \frac{1}{2\pi i} \int_{|z|=\rho} K^{\mathcal{J}} \left( \frac{\|\mathbf{x} - \mathbf{y}\|}{c}, \frac{\gamma(z)}{\Delta_t} \right) z^{-(n+1)} dz$$

where

$$K^{\mathbf{V}} \left( \frac{r}{c}, s \right) = \frac{1}{4\pi r} e^{-\frac{rs}{c}}, \quad K^{\mathbf{K}} \left( \frac{r}{c}, s \right) = -\frac{1}{4\pi r} e^{-\frac{rs}{c}} \left( \frac{1}{r} + \frac{s}{c} \right) \frac{\partial r}{\partial \mathbf{n}_{\mathbf{y}}}, \quad (16)$$

$\gamma(z) = 3/2 - 2z + 1/2z^2$  is the so called characteristic quotient of the chosen BDF method of order 2, and the parameter  $\rho > 0$  is chosen as described below.

By introducing the polar coordinate  $z = \rho e^{i\varphi}$ , the above integrals are efficiently computed by using the trapezoidal rule with  $L \geq N$  equal steps of length  $2\pi/L$ :

$$\omega_n^{\mathcal{J}} \left( \Delta_t; \frac{r}{c} \right) \approx \frac{\rho^{-n}}{L} \sum_{l=0}^{L-1} K^{\mathcal{J}} \left( \frac{r}{c}, \frac{\gamma(\rho \exp(il2\pi/L))}{\Delta_t} \right) \exp(-inl2\pi/L). \quad (17)$$

As suggested in [23] (see also [14]) for the case  $c = 1$ , the choice  $L = 2N$  and  $\rho = 10^{-5/N}$  gives a relative accuracy of order (at least)  $10^{-5} \div 10^{-6}$ . We remark however that for the values of  $c$  we are considering in this paper, the choice  $L = N$  seems to be more than sufficient. For each given  $\mathbf{x} \in \Gamma$ , all the  $\omega_n^{\mathcal{J}}$ ,  $n = 0, \dots, L-1$ , can be computed simultaneously by the FFT, with a number of arithmetic operations proportional to  $L \log L$ . Note that, when one takes  $L > N$ , the required  $\omega_n^{\mathcal{J}}$  are given by the first  $N+1$  components of the coefficient vector, of dimension  $L$ , determined by the FFT.

**Lemma 2.1.** *Let assume that the surface  $\Gamma$  has a parametric representation  $\mathbf{y} = \Psi(\mathbf{u}) = \Psi(u_1, u_2)$ , with  $\Psi \in C^3(\Gamma)$ . Let  $\mathbf{x} = \Psi(\mathbf{v}) = \Psi(v_1, v_2)$ , so that  $r = \|\Psi(\mathbf{v}) - \Psi(\mathbf{u})\|$ . Then, we have*

$$\frac{1}{r} \frac{\partial r}{\partial \mathbf{n}_y} = O(1), \quad r \rightarrow 0$$

*Proof.* Recall the known representation of the gradient vector  $\nabla_y r$ :

$$\nabla_y r = \frac{1}{r} [\Psi(\mathbf{v}) - \Psi(\mathbf{u})]$$

and that of  $\mathbf{n}_y$ :

$$\mathbf{n}_y = \frac{\partial_{u_1} \Psi(\mathbf{u}) \times \partial_{u_2} \Psi(\mathbf{u})}{\|\partial_{u_1} \Psi(\mathbf{u}) \times \partial_{u_2} \Psi(\mathbf{u})\|}.$$

From these we obtain:

$$\frac{\partial r}{\partial \mathbf{n}_y} = \frac{1}{r} \sum_{i=1}^3 (\mathbf{n}_y)_i [\Psi_i(\mathbf{v}) - \Psi_i(\mathbf{u})].$$

Finally, by performing the Taylor expansion

$$\Psi_i(\mathbf{v}) - \Psi_i(\mathbf{u}) = (\mathbf{v} - \mathbf{u})^T \nabla \Psi_i(\mathbf{u}) + \frac{1}{2} (\mathbf{v} - \mathbf{u})^T \mathbf{H}_i (\mathbf{v} - \mathbf{u}) + O(\|\mathbf{v} - \mathbf{u}\|^3)$$

where  $\mathbf{H}_i$  denotes the Hessian matrix associated with the  $i$ -component  $(\Psi)_i = \Psi_i$ , and recalling the property  $\nabla \Psi(\mathbf{u}) \cdot \mathbf{n}_y = 0$ , we easily obtain:

$$\frac{1}{r} \frac{\partial r}{\partial \mathbf{n}_y} = \frac{1}{2} \frac{(\mathbf{v} - \mathbf{u})^T}{r} \left( \sum_{i=1}^3 (\mathbf{n}_y)_i \mathbf{H}_i(\mathbf{u}) \right) \frac{(\mathbf{v} - \mathbf{u})}{r} + O(\|\mathbf{v} - \mathbf{u}\|) = O(1), \quad r \rightarrow 0.$$

□

In view of the next theorem, we recall that the following property

$$\omega_n^{\mathcal{J}} \left( \Delta_t; \frac{r}{c} \right) = \frac{1}{\Delta_t} \omega_n^{\mathcal{J}} \left( 1; \frac{r}{c\Delta_t} \right) \quad (18)$$

holds for the  $\omega_n^{\mathcal{J}}$ -coefficients defined in (15).

**Theorem 2.2.** *Let  $\mathbf{x} \in \Gamma$ ,  $\Delta_t \in \mathbb{R}_+$  be given, and  $r = \|\mathbf{x} - \mathbf{y}\|$ ,  $\mathbf{y} \in \Gamma$ ; furthermore, for notational simplicity, set  $\xi = \frac{r}{c\Delta_t}$ . The  $\omega_n^{\mathcal{J}}(1; \xi)$ -coefficients associated with the operators  $\mathcal{V}$ ,  $\mathcal{K}$  can be simultaneously computed by means of the following recurrence relationship:*

$$\begin{aligned} \omega_1^{\mathcal{V}}(1; \xi) &= \frac{1}{2\pi c} e^{-\frac{3}{2}\xi}, \\ \omega_0^{\mathcal{V}}(1; \xi) &= \frac{\omega_1^{\mathcal{V}}(1; \xi)}{2\xi}, \\ \omega_2^{\mathcal{V}}(1; \xi) &= \left( \xi - \frac{1}{4} \right) \omega_1^{\mathcal{V}}(1; \xi), \\ \omega_n^{\mathcal{V}}(1; \xi) &= \frac{\xi}{n} [2\omega_{n-1}^{\mathcal{V}}(1; \xi) - \omega_{n-2}^{\mathcal{V}}(1; \xi)], \quad n > 2, \end{aligned} \quad (19)$$



and

$$\begin{aligned}
\omega_0^{\mathcal{K}}(1; \xi) &= -\alpha_r \left(1 + \frac{3}{2}\xi\right) \omega_0^{\mathcal{V}}(1; \xi), \\
\omega_1^{\mathcal{K}}(1; \xi) &= -\frac{3}{2}\alpha_r \xi \omega_1^{\mathcal{V}}(1; \xi), \\
\omega_2^{\mathcal{K}}(1; \xi) &= -\frac{\alpha_r}{2}\xi \left(3\xi - \frac{11}{4}\right) \omega_1^{\mathcal{V}}(1; \xi), \\
\omega_n^{\mathcal{K}}(1; \xi) &= -\alpha_r \left[ \left(1 - \frac{n}{2} + \frac{3}{2}\xi\right) \omega_n^{\mathcal{V}}(1; \xi) - \xi \omega_{n-1}^{\mathcal{V}}(1; \xi) \right], \quad n > 2,
\end{aligned} \tag{20}$$

with  $\alpha_r = \frac{1}{r} \frac{\partial r}{\partial \mathbf{n}} = O(1)$ .

*Proof.* The formulas for the  $\omega_n^{\mathcal{V}}$ -coefficients follow immediately from their explicit representation given in [19], [26]:

$$\begin{aligned}
\omega_0^{\mathcal{V}}\left(\Delta_t; \frac{r}{c}\right) &= \frac{1}{4\pi r} e^{-\frac{3r}{2c\Delta_t}}, \\
\omega_n^{\mathcal{V}}\left(\Delta_t; \frac{r}{c}\right) &= \frac{1}{4\pi r n!} e^{-\frac{3r}{2c\Delta_t}} \left(\frac{r}{2c\Delta_t}\right)^{n/2} H_n\left(\sqrt{\frac{2r}{c\Delta_t}}\right), \quad n \geq 1,
\end{aligned} \tag{21}$$

where  $H_n(x) = 2^n x^n + \dots$  is the  $n$ -degree Hermite orthogonal polynomial, and the well-known recurrence relationship  $H_n(x) = 2xH_{n-1}(x) - 2(n-1)H_{n-2}(x)$  (see [1]).

Similar expressions can be easily obtained for the  $\omega_n^{\mathcal{K}}$ -coefficients, starting from the identity  $\omega_n^{\mathcal{K}}(\Delta_t; r/c) = \frac{\partial}{\partial \mathbf{n}} \omega_n^{\mathcal{V}}(\Delta_t; r/c)$  and recalling the relationship  $H'_n(x) = 2nH_{n-1}(x)$  (see [1]). They are:

$$\begin{aligned}
\omega_0^{\mathcal{K}}\left(\Delta_t; \frac{r}{c}\right) &= -\frac{\alpha_r}{4\pi r} e^{-\frac{3r}{2c\Delta_t}} \left(1 + \frac{3r}{2c\Delta_t}\right), \\
\omega_1^{\mathcal{K}}\left(\Delta_t; \frac{r}{c}\right) &= -3\alpha_r \left(\frac{r}{c\Delta_t}\right)^2 \frac{1}{4\pi r} e^{-\frac{3r}{2c\Delta_t}}, \\
\omega_n^{\mathcal{K}}\left(\Delta_t; \frac{r}{c}\right) &= -\alpha_r \left[ \left(1 - \frac{n}{2} + \frac{3r}{2c\Delta_t}\right) \frac{1}{4\pi r n!} e^{-\frac{3r}{2c\Delta_t}} \left(\frac{r}{2c\Delta_t}\right)^{\frac{n}{2}} H_n\left(\sqrt{\frac{2r}{c\Delta_t}}\right) \right. \\
&\quad \left. - \frac{r}{c\Delta_t} \frac{1}{4\pi r (n-1)!} e^{-\frac{3r}{2c\Delta_t}} \left(\frac{r}{2c\Delta_t}\right)^{\frac{n-1}{2}} H_{n-1}\left(\sqrt{\frac{2r}{c\Delta_t}}\right) \right], \quad n \geq 2.
\end{aligned} \tag{22}$$

From these, taking also into account the previous representations of the  $\omega_n^{\mathcal{V}}$ -coefficients, together with identity (18), the expressions given in (19) and (20) follow.  $\square$

Note that, contrary to the approximation (17), under the assumption we have made on  $\xi = \frac{r}{c\Delta_t}$  (see Theorem 2.2) the above recurrence relationships allow to determine the values of the  $\omega_n^{\mathcal{J}}$ -coefficients up to machine accuracy, requiring only very few real arithmetic operations per iteration. Furthermore, once the initial coefficients  $\omega_0^{\mathcal{J}}$ ,  $\omega_1^{\mathcal{J}}$  and  $\omega_2^{\mathcal{J}}$  have been computed, only  $N-2$  iterations need to be performed. Thus, expressions (19) and (20) must be preferred to (17), and we will use them in all the examples reported in Section 4.

**Remark 2.3.** Let  $\Gamma$  be the boundary of a sphere of radius  $R$ . Recalling the representation

$$\frac{\partial r}{\partial \mathbf{n}_y} = \frac{1}{Rr} \sum_{i=1}^3 (y_i - x_i) y_i$$

and using the spherical coordinates, it is quite simple to show, without performing much calculation, that  $\alpha_r = 1/(2R)$ .

**Corollary 2.4.** The coefficients  $\omega_0^{\mathcal{V}}$  and  $\omega_0^{\mathcal{K}}$ , as functions of  $r$ , have an integrable singularity of type  $r^{-1}$ , while all the remaining coefficients are smooth functions. In particular, for all  $n \geq 1$ ,  $\omega_n^{\mathcal{V}}$  and  $\omega_n^{\mathcal{K}}$  are of the type  $e^{-\frac{3r}{2c\Delta_t}} p_{n-1}(\frac{2r}{c\Delta_t})$  and  $\alpha_r e^{-\frac{3r}{2c\Delta_t}} q_n(\frac{2r}{c\Delta_t})$ , respectively, where  $p_{n-1}$  and  $q_n$  are two polynomials of exact degree  $n-1$  and  $n$ .

## 2.2. Approximation in space

For the space discretization, the surface  $\Gamma$  is approximated by a continuous piecewise triangular surface  $\Gamma_\Delta$ , interpolating  $\Gamma$  at the triangle vertices  $\{\mathbf{x}_i, i = 1, \dots, M\}$ . We denote by  $\Delta_x$  the mesh size of  $\Gamma_\Delta$ , which is given by the maximum triangle diameter. We also assume that  $\Delta_x$  is sufficiently small, so that a local parametrization of the surface  $\Gamma$  on each  $\Gamma_\Delta$  triangle can be obtained from that of  $\Gamma$ .

At each time instant  $t_j$ , the unknown function  $u(\cdot, t_j)$  and its normal derivative  $\lambda(\cdot, t_j)$  are approximated by

$$u_{\Delta_x}(\mathbf{x}, t_j) := \sum_{i=1}^M u_i^j b_i(\mathbf{x}), \quad \mathbf{x} \in \Gamma, \quad (23)$$

and

$$\lambda_{\Delta_x}(\mathbf{x}, t_j) := \sum_{i=1}^M \lambda_i^j b_i(\mathbf{x}), \quad \mathbf{x} \in \Gamma, \quad (24)$$

respectively, where  $u_i^j \approx u(\mathbf{x}_i, t_j)$ ,  $\lambda_i^j \approx \lambda(\mathbf{x}_i, t_j)$  and  $\{b_i\}_{i=1}^M$  are the classical continuous piecewise linear basis functions associated with the chosen triangulation.

## 2.3. Time-space discretization

After having introduced the above time and space discretizations, we collocate the resulting discretized BIE at the (collocation) points  $\mathbf{x}_k$ ,  $k = 1, \dots, M$ . To write the final system of equations in vectorial notation, for  $j = 0, \dots, N$  we define the matrices

$$(\mathbf{V}_{n-j})_{ki} = \int_{\Gamma} \omega_{n-j}^{\mathcal{V}} \left( \Delta_t; \frac{\|\mathbf{x}_k - \mathbf{y}\|}{c} \right) b_i(\mathbf{y}) d\Gamma_{\mathbf{y}}, \quad i, k = 1, \dots, M, \quad (25)$$

$$(\mathbf{K}_{n-j})_{ki} = \int_{\Gamma} \omega_{n-j}^{\mathcal{K}} \left( \Delta_t; \frac{\|\mathbf{x}_k - \mathbf{y}\|}{c} \right) b_i(\mathbf{y}) d\Gamma_{\mathbf{y}}, \quad i, k = 1, \dots, M \quad (26)$$

and the vectors

$$\begin{aligned} \mathbf{I}_{u_0}^n &= [I_{u_0}(\mathbf{x}_1, t_n), I_{u_0}(\mathbf{x}_2, t_n), \dots, I_{u_0}(\mathbf{x}_M, t_n)]^T, \\ \mathbf{I}_{v_0}^n &= [I_{v_0}(\mathbf{x}_1, t_n), I_{v_0}(\mathbf{x}_2, t_n), \dots, I_{v_0}(\mathbf{x}_M, t_n)]^T, \\ \mathbf{I}_f^n &= [I_f(\mathbf{x}_1, t_n), I_f(\mathbf{x}_2, t_n), \dots, I_f(\mathbf{x}_M, t_n)]^T. \end{aligned}$$

Then, we introduce the unknown vectors  $\mathbf{u}^j = [u_1^j, \dots, u_M^j]^T$  and  $\boldsymbol{\lambda}^j = [\lambda_1^j, \dots, \lambda_M^j]^T$ , for  $j = 0, \dots, n$ , and obtain the following system of equations (see [14] for the case of a multi domain):

$$\begin{aligned} \left(\frac{1}{2}\mathbf{I} + \mathbf{K}_0\right) \mathbf{u}^n + \sum_{j=0}^{n-1} \mathbf{K}_{n-j} \mathbf{u}^j - \mathbf{V}_0 \boldsymbol{\lambda}^n - \sum_{j=0}^{n-1} \mathbf{V}_{n-j} \boldsymbol{\lambda}^j \\ = \mathbf{I}_{u_0}^n + \mathbf{I}_{v_0}^n + \mathbf{I}_f^n, \quad n = 0, \dots, N, \end{aligned} \quad (27)$$

where  $\mathbf{I}$  denotes the identity matrix of order  $M$ .

From the computational point of view, supposing to know  $\mathbf{u}^j$  and  $\boldsymbol{\lambda}^j$  at the time steps  $j = 0, \dots, n-1$ , the discretized BIE at time  $t_n$  is given by:

$$\left(\frac{1}{2}\mathbf{I} + \mathbf{K}_0\right) \mathbf{u}^n - \mathbf{V}_0 \boldsymbol{\lambda}^n = - \sum_{j=0}^{n-1} \mathbf{K}_{n-j} \mathbf{u}^j + \sum_{j=0}^{n-1} \mathbf{V}_{n-j} \boldsymbol{\lambda}^j + \mathbf{I}_{u_0}^n + \mathbf{I}_{v_0}^n + \mathbf{I}_f^n. \quad (28)$$

The only unknown is  $\boldsymbol{\lambda}^n$  for the Dirichlet problem,  $\mathbf{u}^n$  for a Neumann problem, while for a Dirichlet-Neumann problem the unknowns are  $\boldsymbol{\lambda}^n$  and  $\mathbf{u}^n$ , each one defined in the boundary portion where it is not given.

In the case of the NRBC, in (28), the boundary  $\Gamma$  is replaced by the chosen artificial one, that we denote by  $\mathcal{B}$ , and both  $\mathbf{u}^n$  and  $\boldsymbol{\lambda}^n$  are unknown. Furthermore, in the case of a multiple scattering problem (see [14]) having  $\kappa$  scatterers, each one with its own artificial boundary  $\mathcal{B}_\ell$ , the BIE right hand side (block vector) has the following form:

$$- \sum_{\ell=1}^{\kappa} \sum_{j=0}^{n-1} \mathbf{K}_{n-j}^{i,\ell} \mathbf{u}_{\mathcal{B}_\ell}^j + \sum_{\ell=1}^{\kappa} \sum_{j=0}^{n-1} \mathbf{V}_{n-j}^{i,\ell} \boldsymbol{\lambda}_{\mathcal{B}_\ell}^j + \mathbf{I}_{u_0}^{i,n} + \mathbf{I}_{v_0}^{i,n} + \mathbf{I}_f^{i,n}, \quad i = 1, \dots, \kappa. \quad (29)$$

For each row index, the corresponding row elements of all the above matrices can be computed simultaneously by means of the *FFT* algorithm, after replacing, in the representations (25) and (26), the  $\omega_n^{\mathcal{J}}$  kernel by its discretization (17), and exchanging the integration symbol with that of the quadrature sum (for details see [15]). The computation of the required integrals is performed by using a classical approach based on a  $m$ -point Gauss-Legendre product quadrature, with  $m$  very small.

The evaluation of the volume integrals  $\mathbf{I}_{u_0}^n, \mathbf{I}_{v_0}^n, \mathbf{I}_f^n$  has been discussed in [15]. For simplicity, in the forthcoming numerical tests we will consider only sources concentrated at a point. This choice extremely simplifies the evaluation of the volume term appearing in the BIE.

### 3. Reduction of the BIE computational cost and memory space

For simplicity, we consider a single domain  $\Omega^i$ ; the results we obtain can be easily extended to more general situations of multiple domains.

We recall that till now all the sums

$$\sum_{j=0}^{n-1} \mathbf{K}_{n-j} \mathbf{u}^j, \quad \sum_{j=0}^{n-1} \mathbf{V}_{n-j} \boldsymbol{\lambda}^j, \quad n = 1, \dots, N, \quad (30)$$

are simultaneously computed by applying a FFT-based algorithm (see [7], Sect. 8.3.1), with a computational cost of  $O(M^2 N \log N)$  flops. The required working space, due to the construction of the above matrices  $\mathbf{K}_n, \mathbf{V}_n, n = 0, \dots, N$ , is  $2M^2(N + 1)$ .

In spite of the above statements, in the following we will show that both the computational cost and the required storage can be significantly reduced when the wave propagation velocity is much higher than 1. This reduction is suggested by the behavior of the  $\omega_n^{\mathcal{J}}$ -coefficients stated in Theorem 2.2. Moreover, the smooth behavior of the  $\omega_n^{\mathcal{J}}$ -coefficients, stated in Corollary 2.4, shows that the space integration defined in (25) and (26) can be performed by applying on each triangular element of  $\Gamma_\Delta$  a quadrature formulas with very few nodes (see Remark 3.2 below).

**Theorem 3.1.** *Let  $\Delta_t$  be a given positive real,  $0 < r \leq d$  and  $n = 1, 2, \dots$ . For the  $\omega_n^{\mathcal{J}}$ -coefficients,  $\mathcal{J} = \mathcal{V}, \mathcal{K}$ , the following bounds hold:*

$$r \left| \omega_n^{\mathcal{V}} \left( \Delta_t; \frac{r}{c} \right) \right| < 0.05462 \cdot n^{-\frac{1}{4}} \left( \frac{r}{nc\Delta_t} e^{-\frac{r}{nc\Delta_t} + 1} \right)^{n/2} \quad (31)$$

and

$$r \left| \omega_n^{\mathcal{K}} \left( \Delta_t; \frac{r}{c} \right) \right| < 0.05462 \beta_r^{c\Delta_t} \cdot n^{-\frac{1}{4}} \left( \frac{r}{nc\Delta_t} e^{-\frac{r}{nc\Delta_t} + 1} \right)^{n/2}, \quad (32)$$

where  $\beta_r^{c\Delta_t} = \alpha_r \left( 1 + \frac{1}{2\sqrt{n(n-1)}} + \frac{3r}{c\Delta_t} \right)$ .

*Proof.* Bound (31) follows immediately from (21) in [14], which has been obtained by using representations (21) above, the well-known Stirling's formula for the factorial:

$$n! = \sqrt{2\pi n} n^{n+\frac{1}{2}} e^{-n+\frac{\theta}{12n}}, \quad 0 < \theta < 1,$$

and the bound (see [1], (22.14.17))

$$|H_n(x)| < 1.0865 \cdot 2^{\frac{n}{2}} e^{\frac{x^2}{2}} \sqrt{n!}.$$

Bound (32) follows from representation (22).  $\square$

**Remark 3.2.** *Bound (31), with  $c = 1$ , is identical to that derived in [19], proof of Lemma 4.10. However, in that paper, the authors consider only the single-layer representation and perform the space discretization by a Galerkin method. Furthermore, their main goal is the approximation of the Galerkin matrices by corresponding sparse ones. To this end, they show (see [19], Lemma 4.13) that, for any given (small) real  $\epsilon' > 0$ , when  $r$  is outside the interval  $I_n = [t_n - 3\Delta_t\sqrt{n} \log \epsilon', t_n + 3\Delta_t\sqrt{n} \log \epsilon']$ , it holds*

$$|\omega_n^{\mathcal{V}}(\Delta_t; r)| \leq \frac{\epsilon'}{4\pi r}, \quad n \geq 1.$$

*Thus, for  $\epsilon'$  sufficiently small, under the above assumption on  $r$  the elements of the corresponding matrix become negligible, that is, the matrix itself is negligible.*

We note, however, that for the problems we are considering, being  $r/c > 0$  close to zero, the above mentioned lemma will produce the desired result only for  $n$  sufficiently large, so that  $t_n - 3\Delta_t\sqrt{n}|\log(\epsilon')| > r/c$ . Note also that only when  $n > 9|\log(\epsilon')|^2$  the left hand side of  $I_n$  is positive. For instance, when  $\epsilon' = 10^{-2}, 10^{-3}, 10^{-4}, 10^{-5}, 10^{-6}, 10^{-7}$ , this happens only for  $n \geq 191, 430, 764, 1193, 1718, 2339$ , respectively.

In the following, using our estimates (31) and (32), we will derive a simple expression for a very reasonable cut-off integer  $N_0^{\text{est}}$  (see Definition 3.6 below), such that for all  $n > N_0$  the matrices  $\mathbf{V}_n, \mathbf{K}_n$  are negligible. For instance, in the above mentioned case of Example 1, our estimated values of  $N_0^{\text{est}}$  are smaller than 10.

The following corollary is a straightforward consequence of the above Theorem 3.1.

**Corollary 3.3.** *Let  $c$  and  $\Delta_t$  be fixed, and let  $0 < r \leq d$ , where  $d$  denotes the diameter of the boundary  $\Gamma$  (or of the chosen artificial boundary  $\mathcal{B}$ , in the case of a NRBC). Then, for  $n \rightarrow \infty$ , all elements of the matrices  $\mathbf{V}_n, \mathbf{K}_n$  are bounded by  $\text{const} \cdot n^{-\frac{1}{4}} \left( \frac{d}{nc\Delta_t} e^{-\frac{d}{nc\Delta_t} + 1} \right)^{n/2}$ , where the constant does not depend on  $n, d, c, \Delta_t$ .*

**Remark 3.4.** *From the latter result it follows in particular that, if for the chosen  $\Delta_t$  step-size and some  $N_0 \geq 1$  sufficiently large, we have  $\frac{ed}{N_0 c \Delta_t} (< 1)$  sufficiently small, then for all  $n > N_0$  the corresponding  $\omega_n^{\mathcal{J}}$ -coefficients are negligible. For example, when  $c\Delta_t \geq ed$  and  $n > N_0 = 10$  we have  $n^{-\frac{1}{4}} \left( \frac{d}{nc\Delta_t} e^{-\frac{d}{nc\Delta_t} + 1} \right)^{n/2} < \epsilon = 1.03E - 06$ . Furthermore, the smaller is  $\frac{ed}{c\Delta_t}$ , the smaller is  $N_0$ , i.e., the smaller is the number of significant  $\omega_n^{\mathcal{J}}$ -coefficients. Actually, in some cases it may even happen that only the  $\omega_0^{\mathcal{J}}$ -coefficients are significant.*

On the other end, since  $d, c$  are given values proper of the problem one has to solve, the time step-size  $\Delta_t$  cannot be too small. But for many problems, like those we consider in this paper, this is not a (severe) restriction.

Since from (3) and (4) we obtain

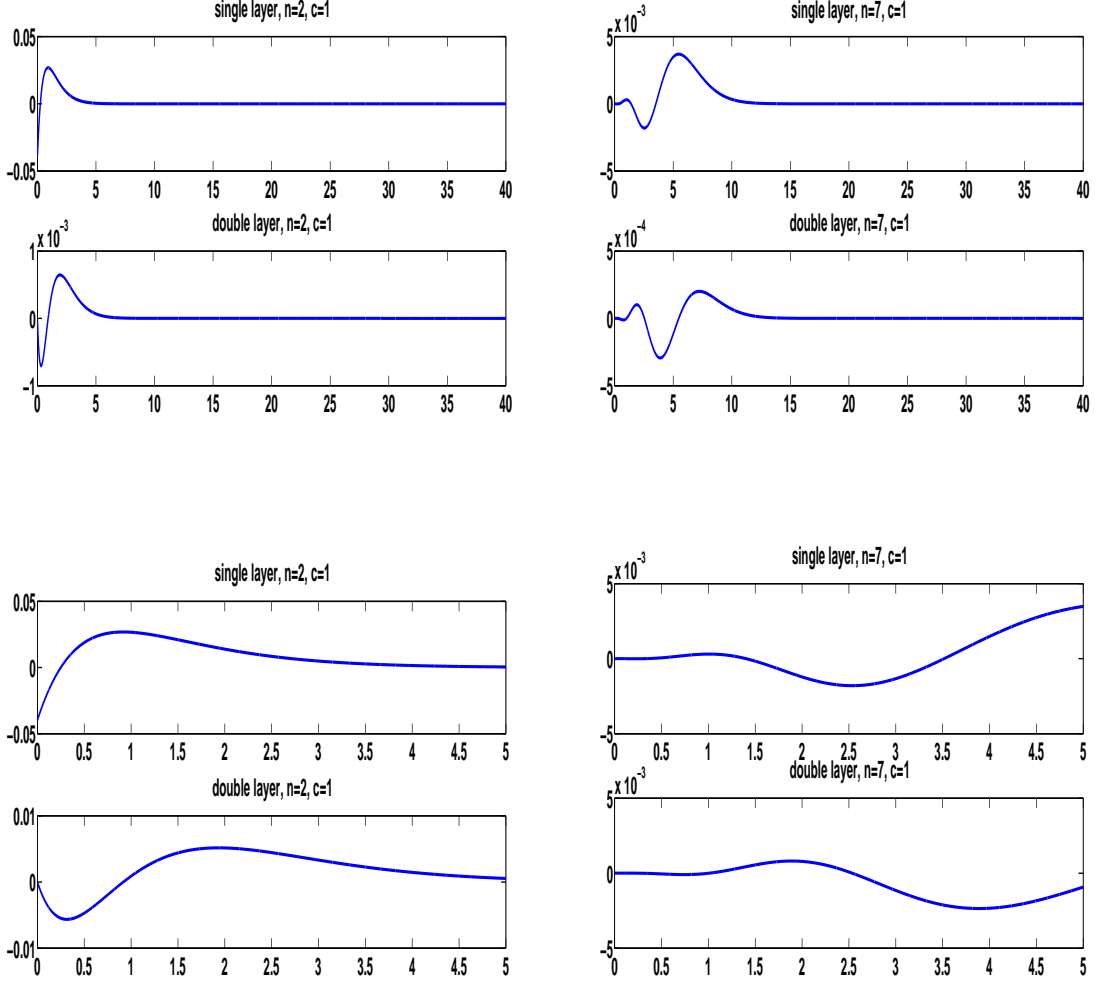
$$\begin{aligned} \mathcal{V}\psi(\mathbf{x}, t_n) &= \int_{\Gamma} \frac{1}{4\pi r} \psi\left(\mathbf{y}, t_n - \frac{r}{c}\right) d\Gamma_{\mathbf{y}} \\ \mathcal{K}\varphi(\mathbf{x}, t_n) &= \int_{\Gamma} \partial_{\mathbf{n}_{\mathbf{y}}} \left( \frac{1}{4\pi r} \varphi\left(\mathbf{y}, t_n - \frac{r}{c}\right) \right) d\Gamma_{\mathbf{y}} \end{aligned}$$

the above behavior of the  $\omega_n^{\mathcal{J}}$ -coefficients, for  $\Delta_t > 0$  fixed and  $n \rightarrow \infty$ , hence of the corresponding matrices, is not unexpected. This because  $\omega_n^{\mathcal{V}}(\Delta_t; r/c)$  appears to represent (see Remark 2 and Fig. 4 in [26]) a smooth “approximation” of the fundamental solution  $G(\cdot, t_n - r/c)$  (see (5) above), and  $\omega_n^{\mathcal{K}}(\Delta_t; r/c) \approx \partial_{\mathbf{n}_{\mathbf{y}}} G(\cdot, t_n - r/c)$ . We also note that the single layer coefficients  $\omega_n^{\mathcal{V}}$  are those which are needed for the solution of the first kind BIE examined in [15]; thus, the same computational reduction can be obtained in that case. An example of this application will be presented in the next section.

Similar bounds could also be obtained for the  $\omega_n$ -coefficients defined by the kernel  $\partial_{\mathbf{n}_{\mathbf{x}}} \partial_{\mathbf{n}_{\mathbf{y}}} G$  of the first kind hypersingular integral equation considered in [8] and [16].

In Figures 1 and 2 we report the behaviors of the coefficients  $\omega_n^{\mathcal{V}}(1; \xi)$  and  $\omega_n^{\mathcal{K}}(1; \xi)$ , for  $n = 2, 7$  (see (15)), when  $\Gamma$  is the surface of the unit sphere. In particular, we have drawn the graphs of  $\omega_n^{\mathcal{V}}(1; \xi)$  (single layer) and  $\omega_n^{\mathcal{K}}(1; \xi)$  (double layer), as functions of  $\xi$ ,  $0 \leq \xi = \frac{r}{c\Delta t} \leq \xi_F$  for the chosen  $\xi_F$ .

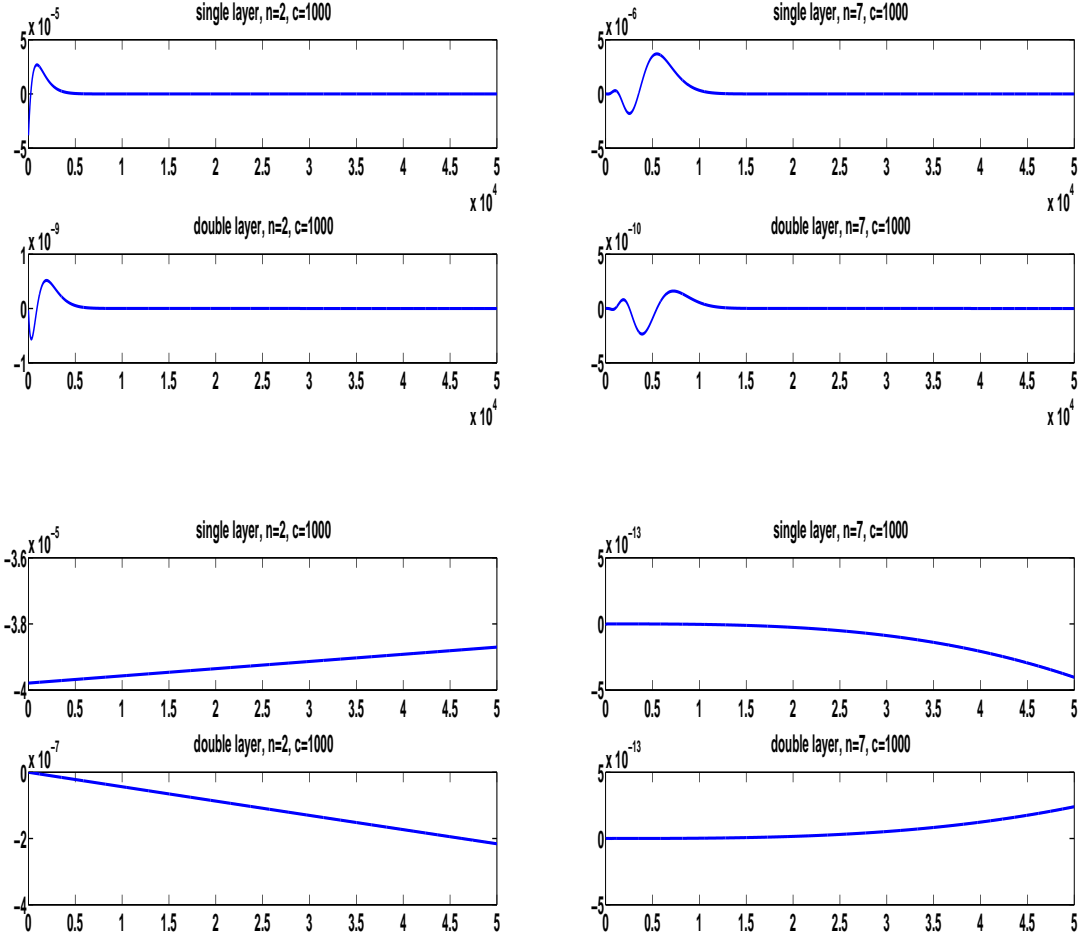
Figure 1: Behavior of the coefficients  $\omega_n^{\mathcal{V}}$ ,  $\omega_n^{\mathcal{K}}$ .



We have obtained very similar graphs also for the  $\omega_n^{\mathcal{J}}$ -coefficients associated with the 2-stage and 3-stage Radau IIA Runge-Kutta methods (see [26]). We recall that for these coefficients, a bound of the type  $\frac{\delta c}{r}(1 - \delta)^{n - \frac{r}{c\Delta t}}$ ,  $n \geq \frac{r}{c\Delta t}$ , for some  $\delta \in (0, 1)$ , has been recently obtained in [4], Proposition 2.2; however, this bound is too crude for our problem, since the constant  $\delta$  does not depend on the velocity  $c$ ; furthermore, it does not allow the definition of a priori estimate of a cut-off integer  $N_0$ .

In the case of the Lubich BDF method of order 1 (see BDF1 in [26]), for the associated

Figure 2: Behavior of the coefficients  $\omega_n^{\mathcal{V}}, \omega_n^{\mathcal{K}}$ .



$\omega_n^{\mathcal{J}}$ -coefficients we have the following very simple representations:

$$\omega_n^{\mathcal{V}}\left(\Delta_t; \frac{r}{c}\right) = \frac{e^{-\frac{r}{c\Delta_t}}}{4\pi r n!} \left(\frac{r}{c\Delta_t}\right)^n > 0, \quad n \geq 0 \quad (33)$$

$$\omega_n^{\mathcal{K}}\left(\Delta_t; \frac{r}{c}\right) = \alpha_r \left(n - 1 - \frac{r}{c\Delta_t}\right) \omega_n^{\mathcal{V}}\left(\Delta_t; \frac{r}{c}\right), \quad n \geq 0. \quad (34)$$

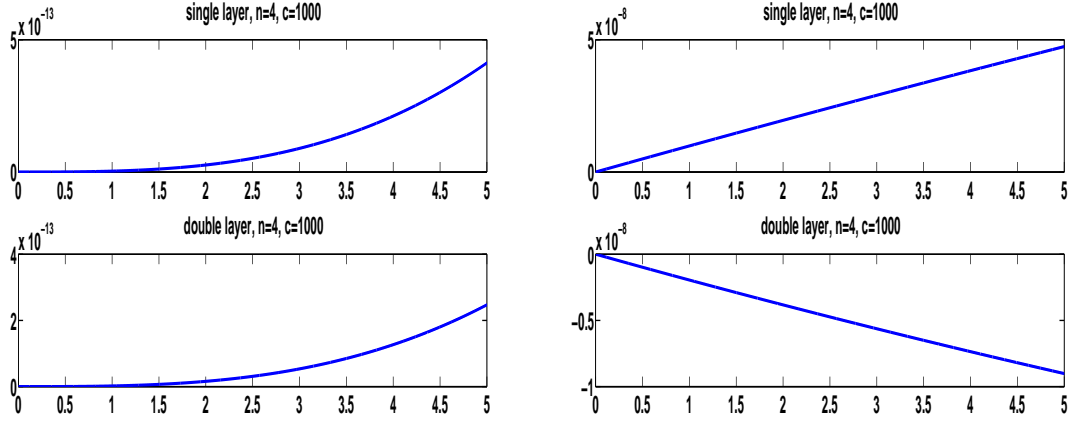
Thus, also for this method we can easily derive bounds very similar to those we have obtained in Corollary 3.3. Actually, the new bounds show a much faster decay to zero, as  $n \rightarrow \infty$ :

$$\omega_n^{\mathcal{V}}\left(\Delta_t; \frac{r}{c}\right) < \frac{e^{-\frac{r}{c\Delta_t}}}{4\pi\sqrt{2\pi}r} n^{-\frac{1}{2}} \left(\frac{ed}{nc\Delta_t}\right)^n, \quad n \geq 1; \quad (35)$$

$$(36)$$

see the graph comparison reported in Figure 3.

Figure 3:  $\omega_n^{\mathcal{J}}$  coefficient ( $\mathcal{J} = \mathcal{V}, \mathcal{K}$ ) comparison between BDF1 (left side) and BDF2 (right side).



**Remark 3.5.** *The major consequence of the results we have obtained above, is that only a very small number of the matrices  $\mathbf{V}_n, \mathbf{K}_n$ , let us say the first  $N_0$ , with  $N_0 \ll N$ , are significant. These, however, are all full, and cannot be approximated by corresponding sparse matrices. Therefore, to solve our propagation problem, we only need to construct and store the first  $N_0$  couple of matrices, being neglected all the remaining ones. Actually, when the velocity is sufficiently high, and the problem sources are not defined by high frequency signals, only the matrices  $\mathbf{V}_0$  and  $\mathbf{K}_0$  turns out to be significant.*

*Another positive consequence, of the proposed truncation, is that the replacement of  $N$  by  $N_0$  in (30) not only reduces significantly the required CPU time and storage, but also makes stable the corresponding sum evaluations (27), (29), no matter how large is  $N$  (as long as  $\Delta_t$  is maintained fixed).*

*Finally, we note that the smaller is  $n$ , the less oscillating are the  $\omega_n^{\mathcal{J}}$ -coefficients (see Figures 2, 3) and the fewer are the quadrature nodes needed to compute, with the required accuracy, the space integrals over each triangular element of  $\Gamma_\Delta$ ; see Section 4. This implies another significant reduction of the computational time.*

We end this section by deriving a criterium to determine an estimate of the truncation integer  $N_0$ , such that, for all  $n > N_0$ , the size of all the elements of the matrices  $\mathbf{V}_n, \mathbf{K}_n$  are less than a given tolerance  $\varepsilon$ . This follows from the bounds of Theorem 3.1 and Remark 3.4. With no practical restrictions, we have assumed that the elements of the chosen surface  $\Gamma_\Delta$ , or at least those having maximum diameters, are equilateral of side  $h$ .

**Definition 3.6.** *Let  $\varepsilon > 0$  a given error threshold, and  $h$  the maximum (triangle) diameter of the  $\Gamma_\Delta$  triangulation under consideration. Then we set  $N_0^{est} = n - 1$ , where  $n$  is the smallest (positive) integer  $n$  satisfying the following couple of inequalities:*

$$n > \frac{d}{c\Delta_t}, \quad 0.052\gamma\nu hn^{-\frac{1}{4}} \left( \frac{d}{nc\Delta_t} e^{-\frac{d}{nc\Delta_t} + 1} \right)^{n/2} < \varepsilon \quad (37)$$



where  $\gamma = 1$  in the case of the single-layer matrices  $\mathbf{V}_n$ ,

$$\gamma = \max_{0 \leq r \leq d} |\alpha_r| \left( 1 + \frac{1}{2\sqrt{n(n-1)}} + \frac{3d}{c\Delta_t} \right)$$

for the double-layer matrices  $\mathbf{K}_n$ , and

$$\gamma = \max \left\{ 1, \max_{0 \leq r \leq d} |\alpha_r| \left( 1 + \frac{1}{2\sqrt{n(n-1)}} + \frac{3d}{c\Delta_t} \right) \right\}$$

in the single-double BIE case. The constant  $\nu$  ( $=6$  in our case) denotes the maximum number of triangles having a common vertex.

Note that  $n > \frac{d}{c\Delta_t}$  means  $t_n > \frac{d}{c}$ , which is in agreement with (3) and (4).

A reasonable choice of the threshold  $\varepsilon$  could be, for example, the accuracy one wants to achieve for his problem solution divided by 100. Furthermore, in the case of the surface of a sphere of radius  $R$ , uniformly partitioned into  $n_\Delta$  plane triangles, we can define  $h = \sqrt{\frac{16\pi}{\sqrt{3}n_\Delta}} R$ . We recall (see Remark 2.3) that when the surface is that of a sphere of radius  $R$ , we have  $\alpha_r = \frac{1}{2R}$ .

The left hand side of the above bound is obtained by considering the worst case among the representations (25) and (26), which one has for  $i = k$ , i.e. when the factor  $1/r$  is (weakly) singular at  $\mathbf{y} = \mathbf{x}_i$ . Moreover, over each (boundary) triangle, the basis function  $b_i(\mathbf{y})$  has been replaced by the constant 1. The above criterium is quite robust with respect to the shape of the  $\Gamma_\Delta$  triangular elements, since the equilateral one represents the worst case. For instance, if one take the triangle having diameter  $h$  and vertices at  $(0, 0)$ ,  $(0, h/\sqrt{2})$ ,  $(h/\sqrt{2}, 0)$ , in the above definition the constant 0.052 must be replaced by 0.022. Of course, more sophisticated and accurate, but less simple, criteria could be derived. To obtain the final expression, we have taken the most crude bounds. Therefore, in general we expect that the integer  $N_0^{est}$  is larger than the true (a posteriori determined)  $N_0$ . In the following examples, we report, for each case considered, both integers  $N_0$  and  $N_0^{est}$ . Note that, the finer is the space discretization, the smaller is  $h$ , hence  $N_0$  and  $N_0^{est}$ .

#### 4. Numerical results

To test the effectiveness of the cutting strategy previously described, in this section we solve several problems of type (1), by using the BEM and the BEM-FEM coupling approaches. Thus, in Example 1, we will solve a test problem by applying our strategy to the BIE (2) and (12), and also to the associated potential representations (in  $\Omega^e$ ) of our PDE problem solution. In particular, we perform this test to check the accuracy of the proposed discretization of (2), since later the first will be used as a NRBC to be coupled with a finite element method.

The problems considered in the subsequent examples will be solved by applying the BEM approach and the BEM-FEM coupling described above. For all the boundary triangulations that have been considered we have  $\nu = 6$  (see Definition 3.6). For simplicity, we have not

devised special strategies to avoid, or at least reduce, the repeated evaluation of the  $\omega_n^{\mathcal{J}}$ -coefficient evaluation at the same quadrature points, when evaluating the elements (25) and (26), or to compute simultaneously the required  $\omega_n^{\mathcal{V}}, \omega_n^{\mathcal{K}}$ .

**Remark 4.1.** *In our numerical testing, integration over the boundary elements is performed by considering the original curved triangles. However, to significantly reduce the method computational cost, without decreasing the BEM overall convergence rate, we replace the  $\Gamma$ -parametrization Jacobian of each curved triangle by that of the associated plane triangle on  $\Gamma_\Delta$ . It can be shown that the (absolute) error due to this approximation is  $O(\Delta_x^4)$ ,  $\Delta_x \rightarrow 0$ . This approximation will however increase the BEM errors, as shown in Example 1, Tables 2,5.*

*We also note that for the single-layer BIE, the accuracy we have obtained by replacing each curved triangle by the associated plane one on  $\Gamma_\Delta$ , is similar to that given by the above mentioned Jacobian approximation. Instead, in the case of the single-double layer BIE, not only errors are much higher, but convergence does not show up clearly. For this reason, in all the examples reported below we have used the “Jacobian approximation” approach.*

Finally, we recall that in all the examples, although not explicitly stated, the unit measures for the physical quantities are: meter (m), second (s) and m/s.

**Example 1.** We consider problem (1), where  $\Omega^i$  is the unit sphere centered at  $(0, 0, 0)$ ,  $u_0 = v_0 = f = 0$  and the Dirichlet boundary datum is of the type  $g(\mathbf{x}, t) = g(t)$ .

First, we solve it by using the approach defined by (12) and (13). In this particular case, the solutions  $\varphi$  and  $u$  are explicitly known:

$$\varphi(\mathbf{x}, t) = \frac{2}{c} \sum_{k=0}^{\lfloor \frac{ct}{2} \rfloor} g' \left( t - \frac{2k}{c} \right), \quad \forall \mathbf{x} \in \Gamma,$$

and, for  $\mathbf{x} \in \Omega^e$ ,

$$u(\mathbf{x}, t) = \begin{cases} 0 & \text{if } t \leq \frac{\|\mathbf{x}\|-1}{c} \\ \frac{1}{\|\mathbf{x}\|} g \left( t - \frac{\|\mathbf{x}\|-1}{c} \right) & \text{otherwise,} \end{cases}$$

and they have been obtained similarly to those in [27] and [14], where they are given for the velocity  $c = 1$ .

In our numerical test we choose

$$g(t) = \frac{1}{2\sqrt{\pi}} t^4 e^{-2t}, \quad t \in [0, 10], \quad c = 1000.$$

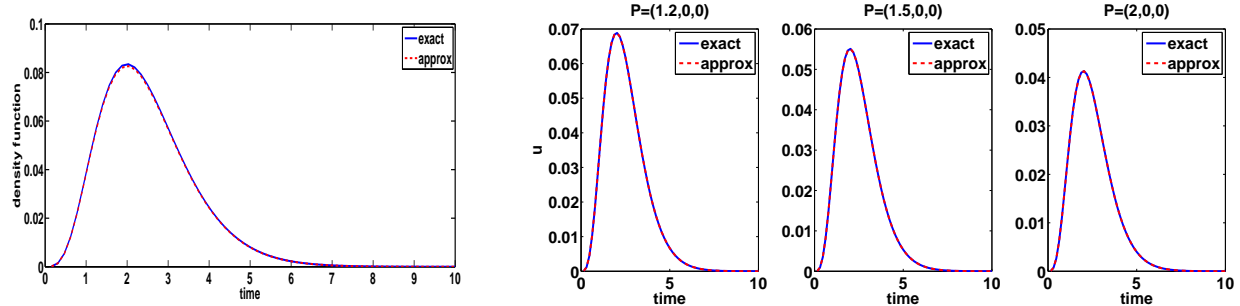
The time interval is divided into  $N$  subintervals. The space domain  $\Gamma$  is approximated by the surface  $\Gamma_\Delta$  of a regular (inscribed) polyhedron having triangular faces, obtained by using the algorithm contained in the software library BEMLIB, which has been downloaded from the internet site: <http://dehesa.freeshell.org/BEMLIB/>. In particular, for the refinement labeled by  $\ell = 1$  we have 32 triangles and 18 vertices, at  $\ell = 2$ : 128 triangles and 66 vertices, at  $\ell = 3$ : 512 triangles and 258 vertices, at  $\ell = 4$ : 2048 triangles and 1026 vertices, and at  $\ell = 5$ : 8192 triangles and 4098 vertices.

The integrals over each  $\Gamma$  triangular face, which define the matrix elements, are computed by using the local surface representation, hence applying the  $8 \times 8$ -point Gauss Legendre quadrature rule. This (fairly high) number of nodes has been chosen to be sure that, by using the same quadrature rule for all discretization refinements, the accuracy of the BEM method does not deteriorate. In some cases (see tables below), this accuracy is of order  $1.0E - 07$  or higher. We remark however that by using a 4-point, degree of exactness 3, rule for the triangle (see [11]), errors up to order  $1.0E - 05$  do not have significant variations. Moreover, in the case of the 2-point rule, only the errors of order less than  $1.0E - 03$  become worse.

Here and in the following,  $\varphi_{\ell,N}(\mathbf{x}, t)$  and  $u_{\ell,N}^S(\mathbf{x}, t)$  denote the approximations of the density function  $\varphi(\mathbf{x}, t)$  and the solution  $u(\mathbf{x}, t)$ , respectively, obtained by (12) and (13), a spatial mesh corresponding to the refinement labeled by  $\ell$  and a temporal mesh of  $N + 1$  equidistant points. Since in the next examples BIE (2) will be used as a NRBC, to be imposed in a strong form, in Tables 4-6 below we also report some pointwise absolute errors associated with these approximations.

In Table 1 we report the absolute errors associated with  $\varphi_{\ell,N}(\mathbf{x}, t)$  at  $t = t_n = T/8, T/4, 3T/8, T/2, 7T/8, T$ ; see also Figure 4. Since, in this example, for fixed  $t$  the density function and its approximation are constant with respect to  $\mathbf{x}$ , here and in the following tables the functions  $\varphi$  and  $\varphi_{\ell,N}$  have been evaluated at the mesh nodal point  $\mathbf{x} = (0, 0, 1)$ .

Figure 4: Example 1. Density function  $\varphi_{2,64}(\mathbf{x}, t)$  (left plot) and solution  $u_{2,64}^S(P, t)$  (right plot), with  $P$  fixed and  $t$  varying.



In the last two columns of Table 1, we also report the maximum of the absolute values  $|\varphi(\mathbf{x}, t_n) - \varphi_{\ell,N}(\mathbf{x}, t_n)|$ ,  $n = 1, \dots, N$ , and the corresponding estimated convergence orders EOC.

All the values reported in Tables 1-3 have been obtained by computing only the matrices  $\mathbf{V}_n$ ,  $n = 0, 1, \dots, N_0 = 4$ , thus neglecting the remaining ones, whose element magnitudes are all smaller than  $1.0E - 08$ . This cutting strategy allows to retrieve, with a significantly lower computational cost and memory space, the same accuracy obtained by using the complete scheme.

Using formula (37), the estimated cutting integer turns out to be  $N_0^{est} = 7$ . This number has been obtained by considering level  $\ell = 5$ , i.e.,  $n_\Delta = 8192$  and  $N = 256$ , although for the accuracy given by the lower levels, a  $1.0E - 08$  threshold is excessively high. In the case of the single-layer operator, represented by the matrix  $\mathbf{V}_n$ , for  $\varepsilon = 1.0E - 05$  we have  $N_0^{est} = 4$ . Using the criterium proposed in [19], recalled above in Remark 3.2, we would have

the cut-off integer  $N_0^{HKS} = 564$  for the latter threshold value, and  $N_0^{HKS} = 1975$  for the former one. These values have been obtained after noting that, to be fair, in the latter rule we must choose  $\epsilon' = 37\epsilon$ . In the following, the cut-off integer obtained by applying to the single-layer matrices  $\mathbf{V}_n$  the criterium defined in [19] will be denoted by  $N_0^{HKS}$ .

To give an idea of the advantages of the cutting strategy, we remark that, for example, we could not apply the numerical method with the parameters of level  $\ell = 5$ , since the required memory space was prohibitive for our PC. On the contrary, we could perform  $\ell = 5$  with  $N_0 = 4$ , obtaining numerical results which preserve the expected order of convergence. Moreover, the CPU time required by the method with the cutting strategy is significantly reduced with respect to that of the complete method with  $N_0 = N$ , especially when  $N$  is large. Indeed, in the simple case we have considered here, where  $N$  is relatively small, the use of  $N_0 = 4$  instead of  $N = 16, 32, 64, 128$  allows to obtain a reduction of the computational time of 0.5%, 20%, 35% and 49%, respectively.

Table 1: Example 1. Absolute errors  $|\varphi(\mathbf{x}, t) - \varphi_{\ell, N}(\mathbf{x}, t)|$ ,  $N_0 = 4$ .

$\ell$	$N$	$T/8$	$T/4$	$3T/8$	$T/2$	$7T/8$	$\max_t$	EOC
1	16	$9.12E-03$	$1.19E-02$	$4.95E-03$	$1.29E-03$	$6.70E-06$	$1.32E-02$	2.02
2	32	$2.26E-03$	$2.95E-03$	$1.23E-03$	$3.18E-04$	$1.66E-06$	$3.26E-03$	
3	64	$5.43E-04$	$7.09E-04$	$2.95E-04$	$7.66E-05$	$3.98E-07$	$7.90E-04$	2.04
4	128	$1.23E-04$	$1.60E-04$	$6.67E-05$	$1.73E-05$	$9.01E-08$	$1.79E-04$	2.14
5	256	$1.93E-05$	$2.52E-05$	$1.05E-05$	$2.74E-06$	$1.43E-08$	$2.81E-05$	2.67

In Table 2 we report the (approximated)  $L^2$ -norm absolute errors for some values of  $t$ , given by  $\|\varphi(\cdot, t) - \varphi_{\ell, N}(\cdot, t)\|_{L^2(\Gamma)}$ , where the integral on each triangle  $\mathcal{T} \in \Gamma$  is first approximated as described in Remark 4.1, and then computed by using the 4-point quadrature rule of order 3 taken from [11]. As in the previous table, we report first the errors at five instants, and then its maximum with respect to all computational instants, together with the associated EOC. The last column, identified by the symbol  $J_{\tilde{\Delta}}$ , contains the corresponding maximum errors obtained by computing all integrals defined on the  $\Gamma$  triangles by using the exact triangle representation Jacobian. In this latter case, because of the higher accuracy one can obtain, we had to take  $N_0 = 5$ . This same procedure has also been applied to obtain the results reported in Table 5 below.

Table 2: Example 1. Absolute errors  $\|\varphi(\cdot, t) - \varphi_{\ell, N}(\cdot, t)\|_{L^2(\Gamma)}$ ,  $N_0 = 4$ .

$\ell$	$N$	$T/8$	$T/4$	$3T/8$	$T/2$	$7T/8$	$\max_t$	EOC	$\max_t, J_{\tilde{\Delta}}$
1	16	$3.37E-02$	$4.40E-02$	$1.83E-02$	$4.75E-03$	$2.47E-05$	$4.87E-02$	1.82	$1.05E-04$
2	32	$9.58E-03$	$1.25E-02$	$5.20E-03$	$1.35E-03$	$7.02E-06$	$1.38E-02$		$3.66E-05$
3	64	$2.52E-03$	$3.29E-03$	$1.37E-03$	$3.55E-04$	$1.84E-06$	$3.66E-03$	1.91	$1.17E-05$
4	128	$6.44E-04$	$8.42E-04$	$3.50E-04$	$9.08E-05$	$4.72E-07$	$9.37E-04$	1.97	$3.47E-06$
5	256	$1.64E-04$	$2.15E-04$	$8.94E-05$	$2.32E-05$	$1.21E-07$	$2.39E-04$	1.97	$2.00E-06$

Note that the EOC reported in the above tables confirm the expected second order convergence rate (see [15]).

In Table 3 we report the maximum value of the absolute errors  $|u(\mathbf{x}, t_n) - u_{\ell,N}^S(\mathbf{x}, t_n)|$ ,  $n = 1, \dots, N$ , at some fixed points  $\mathbf{x} = P$ , and the corresponding EOC. Note that the approximant  $u_{\ell,N}^S$  shows a third order super convergent behavior.

Table 3: Example 1. Absolute errors  $\max_t |u(P, t) - u_{\ell,N}^S(P, t)|$ ,  $N_0 = 4$ .

$\ell$	$N$	$P = (1.01, 0, 0)$	EOC	$P = (1.5, 0, 0)$	EOC	$P = (2, 0, 0)$	EOC
1	16	$5.00E-05$	0.91	$9.15E-04$	2.91	$7.47E-04$	2.94
2	32	$2.67E-05$	1.70	$1.22E-04$	3.03	$9.71E-05$	3.04
3	64	$8.22E-06$	2.91	$1.49E-05$	3.07	$1.18E-05$	3.02
4	128	$1.09E-06$	2.63	$1.78E-06$	3.69	$1.45E-06$	3.41
5	256	$1.76E-07$		$1.38E-07$		$1.36E-07$	

Finally, we solve the same problem by applying the approach described in Section 2, taking also in this case  $N_0 = 4$ ; we denote by  $\lambda_{\ell,N}$  and  $u_{\ell,N}^{SD}$  the approximation of  $\lambda$  and  $u$  respectively, obtained by solving (2) on  $\Gamma$  and computing (11). In Tables 4-6 we report the numerical results obtained for the unknown density function  $\lambda(\mathbf{x}, s) = \partial_{\mathbf{n}} u(\mathbf{x}, s)$  and for  $u(\mathbf{x}, t)$ . Also in this case, the first five matrices ( $N_0 = 4$ ) for both the single and the double layer operators, are sufficient to obtain the same accuracy one would obtain by considering all the  $N$  matrices.

Table 4: Example 1. Absolute errors  $|\lambda(P, t) - \lambda_{\ell,N}(P, t)|$  at  $P = (0, 0, 1)$ ,  $N_0 = 4$ .

$\ell$	$N$	$T/8$	$T/4$	$3T/8$	$T/2$	$7T/8$	$\max_t$	EOC
1	16	$4.57E-03$	$5.95E-03$	$2.47E-03$	$6.43E-04$	$3.37E-06$	$6.60E-03$	2.02
2	32	$1.13E-03$	$1.47E-03$	$6.13E-04$	$1.59E-04$	$8.32E-07$	$1.63E-03$	2.04
3	64	$2.73E-04$	$3.54E-04$	$1.47E-04$	$3.83E-05$	$2.00E-07$	$3.95E-04$	2.15
4	128	$6.17E-05$	$8.02E-05$	$3.34E-05$	$8.69E-06$	$4.53E-08$	$8.93E-05$	2.59
5	256	$1.01E-05$	$1.34E-05$	$5.62E-06$	$1.47E-06$	$7.72E-09$	$1.48E-05$	

Table 5: Example 1. Absolute errors  $\|\lambda(\cdot, t) - \lambda_{\ell,N}(\cdot, t)\|_{L^2(\Gamma)}$ ,  $N_0 = 4$ .

$\ell$	$N$	$T/8$	$T/4$	$3T/8$	$T/2$	$7T/8$	$\max_t$	EOC	$\max_t, J_{\tilde{\Lambda}}$
1	16	$1.69E-03$	$2.20E-02$	$9.14E-03$	$2.38E-03$	$1.24E-05$	$2.44E-02$	1.82	$1.03E-04$
2	32	$4.81E-03$	$6.25E-03$	$2.60E-03$	$6.75E-04$	$3.52E-06$	$6.92E-03$	1.92	$3.47E-05$
3	64	$1.26E-03$	$1.64E-03$	$6.83E-04$	$1.78E-04$	$9.24E-07$	$1.83E-03$	1.96	$1.17E-05$
4	128	$3.23E-04$	$4.21E-04$	$1.75E-04$	$4.55E-05$	$2.37E-07$	$4.69E-04$	1.94	$3.15E-06$
5	256	$8.36E-05$	$1.09E-04$	$4.59E-05$	$1.19E-05$	$6.23E-08$	$1.22E-04$		$3.96E-06$

By comparing the results reported in Tables 3 and 6 we note the superiority of the single-layer approach proposed in [15]. For example, in Table 3, the errors obtained by taking  $\ell = 1$ ,  $N = 16$  and  $\ell = 3$ ,  $N = 64$  are smaller than those reported in Table 6 for  $\ell = 2$ ,  $N = 32$  and  $\ell = 5$ ,  $N = 256$ , respectively. The single-layer operator apparently increases by one order the convergence rate of the density approximant. This is probably due to the higher order smoothing effect of the single-layer operator with respect to the double-layer one (see [28]). Unfortunately, the single-layer BIE cannot be used to define a non reflection boundary condition to be coupled with a finite element or finite difference method.

Table 6: Example 1. Absolute errors  $\max_t |u(P, t) - u_{\ell, N}^{SD}(P, t)|$ ,  $N_0 = 4$ .

$\ell$	$N$	$P = (1.01, 0, 0)$	EOC	$P = (1.5, 0, 0)$	EOC	$P = (2, 0, 0)$	EOC
1	16	$1.45E - 02$		$4.61E - 03$		$3.77E - 03$	
			1.79		1.83		1.89
2	32	$4.18E - 03$		$1.30E - 03$		$1.02E - 03$	
			3.11		1.97		1.97
3	64	$4.84E - 04$		$3.31E - 04$		$2.60E - 04$	
			3.72		2.00		2.00
4	128	$3.67E - 05$		$8.26E - 05$		$6.48E - 05$	
			1.24		1.97		1.91
5	256	$1.55E - 05$		$2.11E - 05$		$1.72E - 05$	

In the following examples, we consider the BEM-FEM coupling method for the solution of Problem (1), by applying the cutting strategy introduced in the previous sections. In particular, we solve wave propagation problems in the case of waves generated by incident fields or external sources. We will see that, as in the BEM approach, the cutting strategy performs well in the BEM-FEM coupling too, producing the same order of accuracy of the complete scheme and with no spurious reflections.

Since in the examples we consider next the corresponding exact solution is not known, to measure the accuracy of the approximations we obtain, we construct a reference “exact” solution as follows: we first solve the single layer BIE (12) on a fine space and time discretization with no cutting; then, we retrieve the solution at any point in the infinite domain  $\Omega^e$  by computing the associated potential (13). This solution will be denoted by  $u^S$ .

For what concerns the BEM-FEM method, we remark that the discretization of the three dimensional spatial domain  $\Omega$  is generated by using the Freefem++ library. In particular we use the TetGen software, which allows to generate the tetrahedral mesh of the domain  $\Omega$  starting from that we define on its boundary. The finite computational domains that we will consider for our numerical examples are three dimensional shells bounded internally by a surface  $\Gamma$  and externally by a surface  $\mathcal{B}$ . The shell discretization, which is constructed by TetGen, is a three dimensional Piecewise Linear Complex (PLC), having an internal boundary  $\Gamma_\Delta$  and an external one  $\mathcal{B}_\Delta$ . In what follows,  $n_T$  denotes the number of tetrahedra of the PLC domain discretization, while  $n_{\Delta, \Gamma}$  and  $n_{\Delta, \mathcal{B}}$  denote the number of triangles belonging to the boundaries  $\Gamma_\Delta$  and  $\mathcal{B}_\Delta$ , respectively.

In the forthcoming numerical test, we solve each problem by using the BEM and/or BEM-FEM approaches; whenever the results are very similar, we report only those obtained by the latter one. We remark that, for the BEM-FEM coupling approach, in all the numerical tests the evaluation of the entries of the matrices involved in the NRBC has been performed by

a 2-point Gauss-Legendre quadrature product formula; this choice revealed to be sufficient for qualitatively accurate plots.

**Example 2. Case a).** We consider the scattered field of a plane wave impinging upon a sphere of radius 1 with velocity  $c = 343$ . The incident wave

$$u^{inc}(\mathbf{x}, t) = e^{-2 \cdot 10^{-2}(x_1 - 400 + ct)^2}$$

is centered at the point  $\mathbf{x}_0 = (400, 0, 0)$  and propagates along the  $x_1$ -axis to the left direction. The total wave field  $u^{tot}$  is given by the sum of the incident wave  $u^{inc}$  and the scattered one  $u^{scat}$ , where the latter is the solution of (1) with the Dirichlet datum  $g(\mathbf{x}, t) = -u^{inc}(\mathbf{x}, t)$  on the boundary  $\Gamma$  of the unit sphere.

We approximate  $u^{tot}$  by using the BEM-FEM approach, in the domain  $\Omega$  bounded internally by  $\Gamma$  and externally by the artificial boundary  $\mathcal{B}$ , chosen as the surface of a sphere of radius 2. We choose a decomposition of  $\Omega$  into  $n_T = 32368$  tetrahedra and  $n_{\Delta, \mathcal{B}} = 1772$  triangles, and a discretization of the time interval  $[0, 3]$  into  $N = 1024$  subintervals. We have considered the cutting parameter  $N_0 = 14$  ( $N_0^{est} = 21$ ), which corresponds to the threshold value  $\varepsilon = 1.0E - 05$ . We recall that a smaller value of  $N_0$  does not deteriorate the qualitative accuracy of the graph. For completeness, we report the percentage of the ratios of the CPU times and of the memory spaces required by the numerical method, when the cutting strategy is compared with the complete scheme. In particular, we consider the CPU times for the computation of the matrices involved in the discretization of the NRBC (in the sequel denoted by CPU-mat) and the CPU times required for the computation of the right hand side term of (28) (denoted by CPU-rhs). In this case, we have CPU-mat= 0.1% and CPU-rhs= 3%, while the ratio of the memory space is 1%.

In Figure 5, we show the behavior of the total field  $u^{tot, BF}$  computed by the BEM-FEM coupling method at the point  $P \approx (2, 0, 0)$ , belonging to the artificial boundary  $\mathcal{B}$  (left plot). In the middle and right plots we show the associated absolute errors  $|u^{tot, S}(P, t) - u^{tot, BF}(P, t)|$  and energy, respectively. The reference solution  $u^{tot, S}$  has been obtained by a complete BEM approach with a discretization of the boundary  $\Gamma$  into  $n_{\Delta, \Gamma} = 1772$  triangles, and of the time interval into  $N = 2048$  subintervals. We point out that, in the BEM-FEM coupling, the energy test is important to reveal the eventual presence of spurious reflections in case of evanescent waves. In this case, the energy dissipates as expected even when the cutting strategy is applied.

**Case b).** For the same geometrical setting and velocity of Case a), we consider the incident wave packet

$$u^{inc}(\mathbf{x}, t) = \sum_{i=1}^6 e^{-2(x_1 - \xi_i + ct)^2},$$

with  $\xi_i = 50, 55, 60, 65, 70, 75$ , consisting of a sum of six successive waves spaced at regular intervals. We solve the problem by using the BEM approach. The time interval of interest  $[0, 0.4]$  has been subdivided into  $N = 2048$  subintervals; the unit sphere has been discretized with the spatial refinement  $\ell = 3$  ( $n_{\Delta, \Gamma} = 512$ ).

We remark that the chosen fine time discretization is necessary to reproduce the very narrowed and picked behavior of the wave, as Figure 7 shows, where the behaviors of incident, scattered and total fields are represented at some points  $P$  with respect to the time variable.



Figure 5: Example 2, Case a). Total field at  $P \approx (2, 0, 0)$  (left plot), absolute error (middle plot), energy (right plot),  $N = 1024$ ,  $N_0 = 14$ .

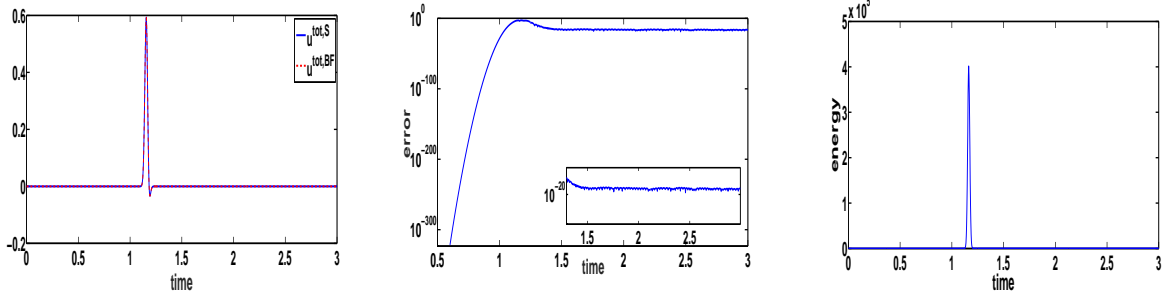
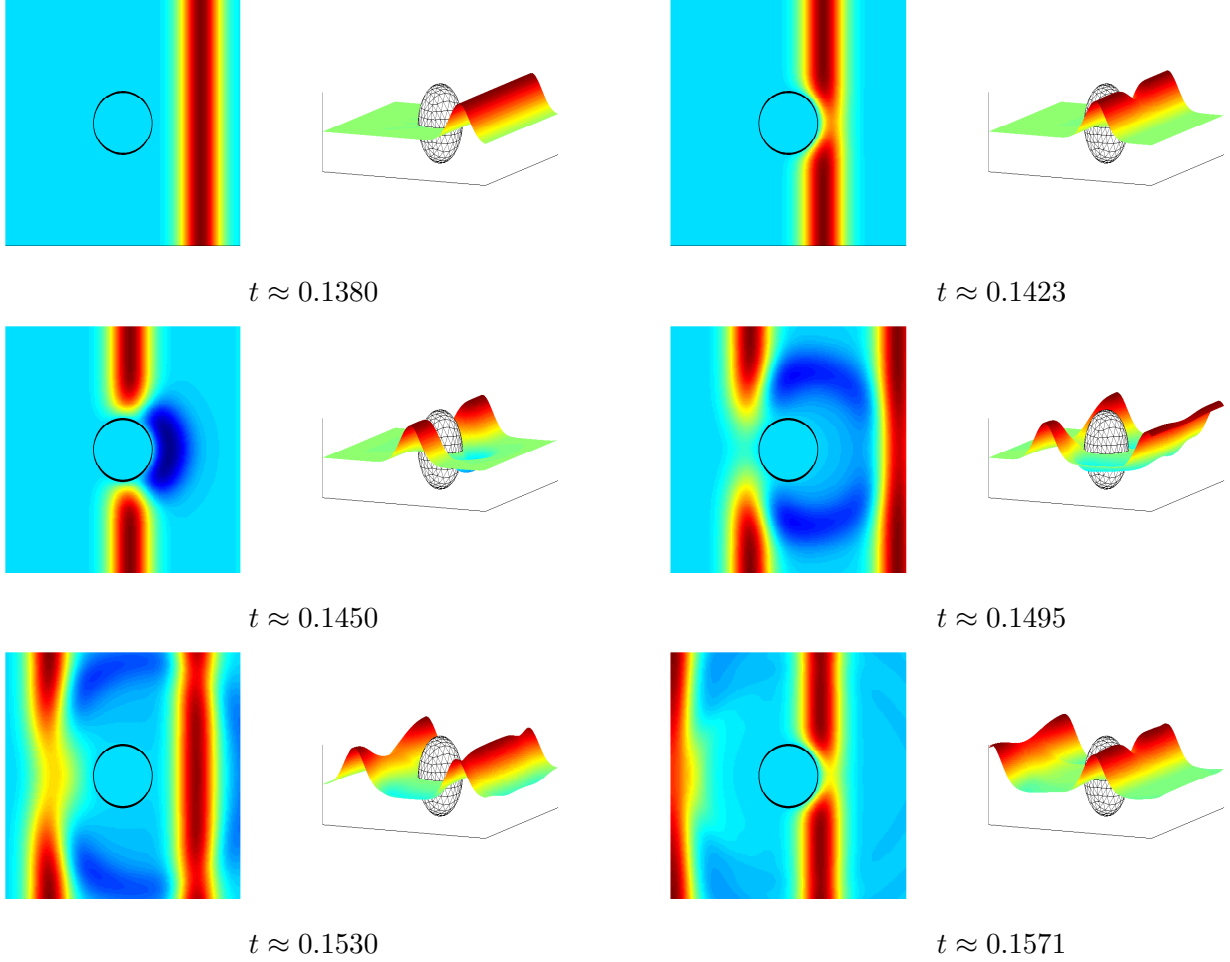
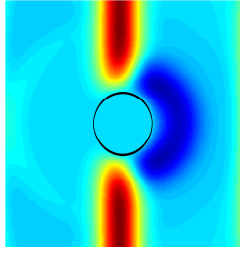


Figure 6: Example 2, Case b). Snapshots of the solution at different instants.

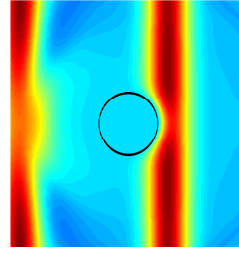
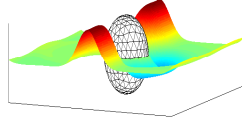


In Figure 6 we show the 2D and 3D snapshots of the total field at different instants and at the  $x_1x_2$ -domain  $[-4, 4] \times [-4, 4]$ , external to the obstacle. In all the numerical tests the cutting parameter is  $N_0 = 71$  ( $N_0^{est} = 88$ ), corresponding to the error threshold  $\varepsilon = 1.0E-08$ . We have obtained the same graphs by setting  $\varepsilon = 1.0E-05$ , for which we have  $N_0 = 54$  and  $N_0^{est} = 74$ .

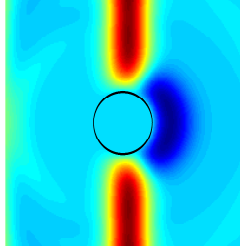
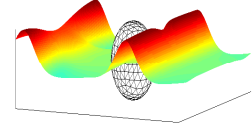




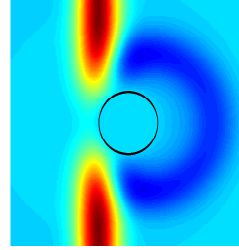
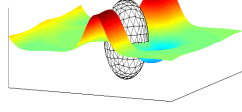
$t \approx 0.1606$



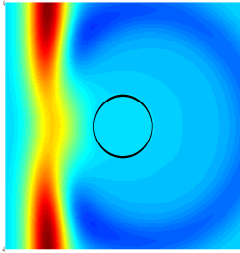
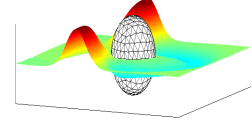
$t \approx 0.1710$



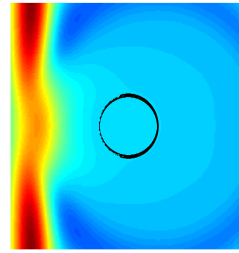
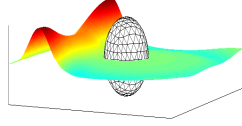
$t \approx 0.2181$



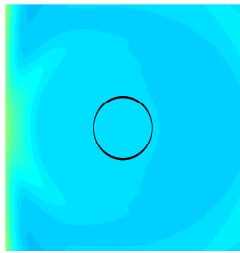
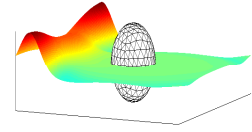
$t \approx 0.2216$



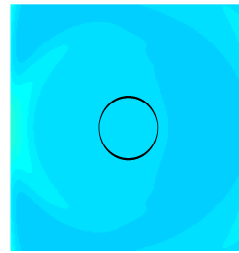
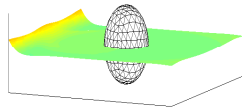
$t \approx 0.2261$



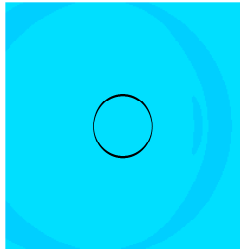
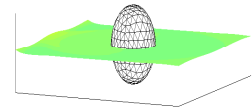
$t \approx 0.2282$



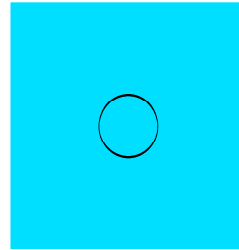
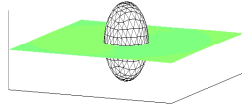
$t \approx 0.2325$



$t \approx 0.2335$



$t \approx 0.2380$



$t \approx 0.2730$

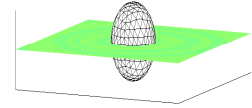
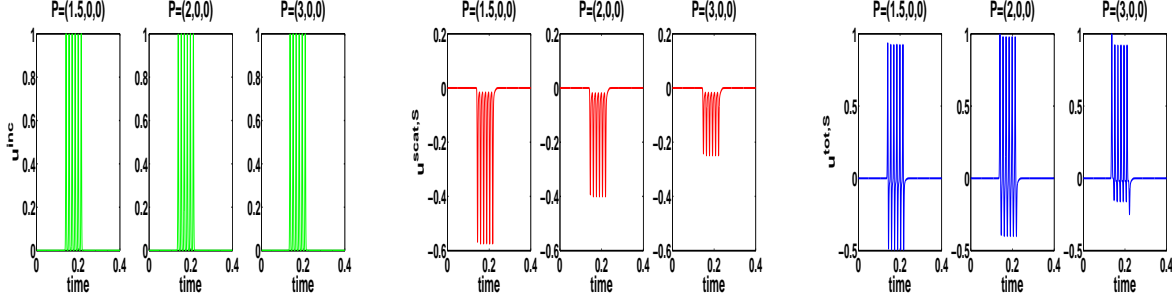


Figure 7: Example 2, Case b). Incident (left plot), scattered (middle plot) and total (right plot) field at some points  $P$ ,  $N = 2048$ ,  $N_0 = 54$ .



If we consider solely the single-layer matrices  $\mathbf{V}_n$ , with error tolerances  $\varepsilon = 1.0E - 05$ ,  $1.0E - 08$ , then our estimate (37) gives  $N_0^{est} = 65, 80$ , respectively, while the corresponding values obtained using the [19] criterium, after setting  $\epsilon' = 9.2462\varepsilon$ , are  $N_0^{HKS} = 834, 2420$ .

**Example 3.** We consider a wave generated by a source  $f$ , impinging upon a soft obstacle. The data of the problem are  $u_0 = 0$ ,  $v_0 = 0$ ,  $g = 0$ .

**Case a).** As a first case, we consider a point source

$$f(\mathbf{x}, t) = h(t)\delta(\mathbf{x} - \mathbf{x}_0), \quad \mathbf{x}_0 = (5, 0, 0), \quad h(t) = e^{-(t-5)^2} \cos(60t).$$

For this example we consider the BEM-FEM approach. The obstacle is the unit sphere and the artificial boundary  $\mathcal{B}$  is the surface of the sphere centered at  $(0, 0, 0)$  and of radius 2. With this choice, the contribution of the source  $f$ , which is located out of the finite computational domain, is taken into account by the volume term  $I_f$  defined by (8). Because of the presence of the delta Dirac function in the expression of the fundamental solution, the volume integral  $I_f$  has the following simple expression:

$$I_f(\mathbf{x}, t) = \begin{cases} \frac{h\left(t - \frac{\|\mathbf{x} - \mathbf{x}_0\|}{c}\right)}{4\pi\|\mathbf{x} - \mathbf{x}_0\|} & \text{for all } \mathbf{x} : \frac{\|\mathbf{x} - \mathbf{x}_0\|}{c} < t \\ 0 & \text{otherwise.} \end{cases} \quad (38)$$

The velocity is  $c = 1500$ , which refers to the propagation of seismic or acoustic waves in the water. In Figure 8, we show the behavior of the solution  $u^{BF}$  obtained by the BEM-FEM coupling at a point  $P \approx (2, 0, 0)$  in the time interval  $[0, 10]$ , and the associated absolute error  $|u^S(P, t) - u^{BF}(P, t)|$ , where the BEM reference solution  $u^S$  has been obtained by a discretization of the unit sphere into  $n_{\Delta, \Gamma} = 1770$  triangles. The solution  $u^{BF}$  has been computed by a decomposition of the shell into  $n_T = 32368$  tetrahedra; the triangular mesh inherited on the artificial boundary  $\mathcal{B}$  consists of  $n_{\Delta, \mathcal{B}} = 1772$  triangles. In both cases the time interval  $[0, 10]$  has been subdivided into  $N = 2048$  subintervals; this choice allows to obtain a good approximation of the highly oscillating behavior (in time) of the solution.

Besides applying the cutting strategy to the BEM-FEM approach, with  $N_0 = 4$  ( $N_0^{est} = 9$ ), corresponding to the threshold  $\varepsilon = 1.0E - 05$ , we have performed truncation also in the BEM approach with the same value of  $N_0$  ( $N_0^{est} = 6$ ). We remark that, for a good approximation of  $u^S$ , with or without cutting, it is sufficient to consider a coarse triangular

decomposition of  $\Gamma$ . On the contrary, a decomposition of the shell coarser than that we have considered, consisting of  $n_T = 7792$  tetrahedra and  $n_{\Delta, \mathcal{B}} = 440$  triangles, deteriorates the accuracy of the solution  $u^{BF}$  (see Figure 9). This is due exclusively to the finite element computation; indeed, based on an intensive numerical testing, the accuracy of the  $u^{BF}$  solution does not improve by taking a higher number of quadrature nodes, for the computation of the matrix elements, and a smaller cutting parameter  $\varepsilon$ . Incidentally, we remark that the cutting strategy revealed to be crucial in this case, since the complete scheme with  $n_T = 32368$  and  $N_0 = 2048$  could not run on our PC because of an out of memory. For completeness, in the right plot we show the behavior of the energy of the system. As expected, the energy is null until the wave generated by the external source reaches the computational domain, it oscillates as a consequence of the oscillating behavior of the wave, and it decays to zero when the wave leaves the computational domain since the source  $f$  is evanescent.

Figure 8: Example 3, case a). Solution  $u^{BF}(P, t)$  at  $P \approx (2, 0, 0)$  (left plot), associated absolute error (middle plot), and energy of the system (right plot),  $n_T = 32368$ ,  $n_{\Delta, \mathcal{B}} = 1772$ ,  $N = 2048$ ,  $N_0 = 4$ .

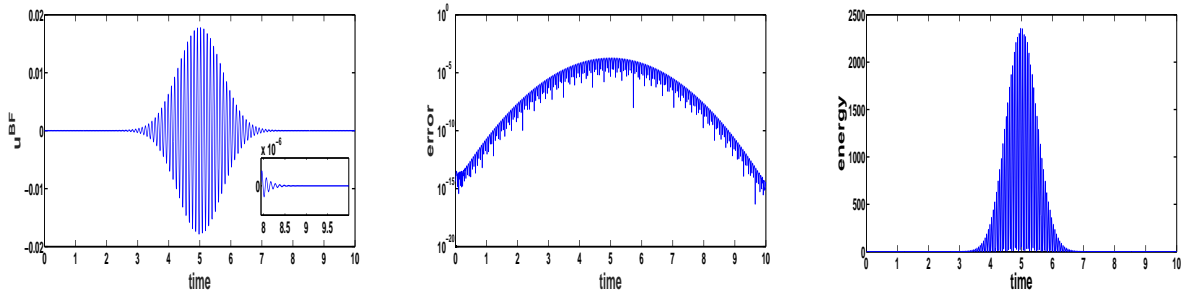
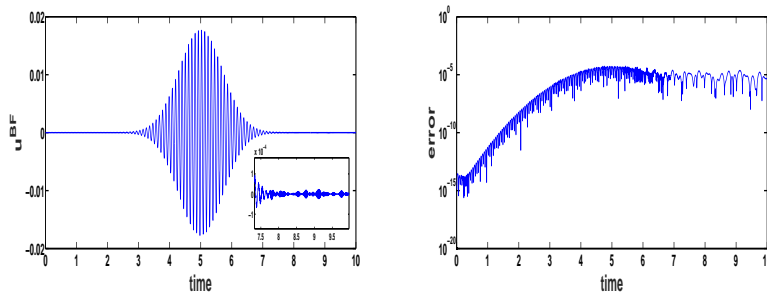


Figure 9: Example 3, case a). Solution  $u^{BF}(P, t)$  at  $P \approx (2, 0, 0)$  (left plot) and associated absolute error (right plot),  $n_T = 7792$ ,  $n_{\Delta, \mathcal{B}} = 440$ ,  $N = 2048$ ,  $N_0 = 4$ .



**Case b).** The second example we consider is a wave generated by a point source, traveling with velocity  $c = 3000$  towards a large spherical obstacle of radius  $r = 100$ . More precisely, we choose

$$f(\mathbf{x}, t) = h_1(t)\delta(\mathbf{x} - \mathbf{x}_0), \quad \mathbf{x}_0 = (6100, 0, 0), \quad h_1(t) = 10^5 e^{-(10t)^2} \sin(6t).$$

In Figure 10 we show the behavior of the solution  $u^S$  at some point  $P$  of the exterior domain, computed by the BEM approach with  $\ell = 2$  (space discretization),  $N = 1024$  (time discretization) and cutting parameter  $N_0 = 41$  ( $N_0^{est} = 48$ ) defined by the threshold  $\varepsilon = 1.0E - 05$ . The time interval of integration is  $[0, 5]$ . In this case, to apply the [19] rule, the proper value of  $\epsilon'$  is  $4.6232E - 07$ , and we have  $N_0^{HKS} = 1942$ .

In this particular example, we observe that the incident wave reaches the points  $P = (200, 0, 0)$ ,  $P = (500, 0, 0)$ ,  $P = (1000, 0, 0)$  at the instants  $t \approx 1.7, 1.87, 1.97$ , respectively; then it is reflected back by the obstacle and the scattered wave is clearly visible in each plot.

In Figure 11, by assuming as reference values the ones obtained by the complete BEM scheme, 8-point Gauss-Legendre quadrature product formula and  $\ell = 3$  spatial discretization, we report the absolute error associated to the solution obtained by the partial scheme.

Figure 10: Example 3, case b). Solution  $u^S(P, t)$  for  $h_1$  at some  $P$ ,  $N = 1024$ ,  $N_0 = 41$ .

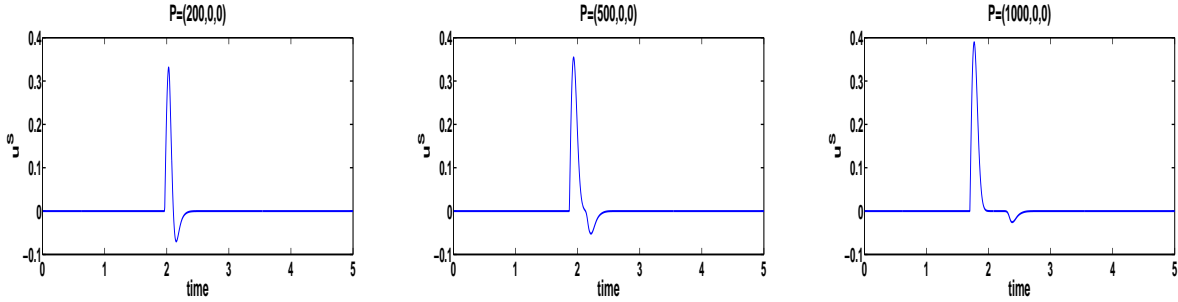
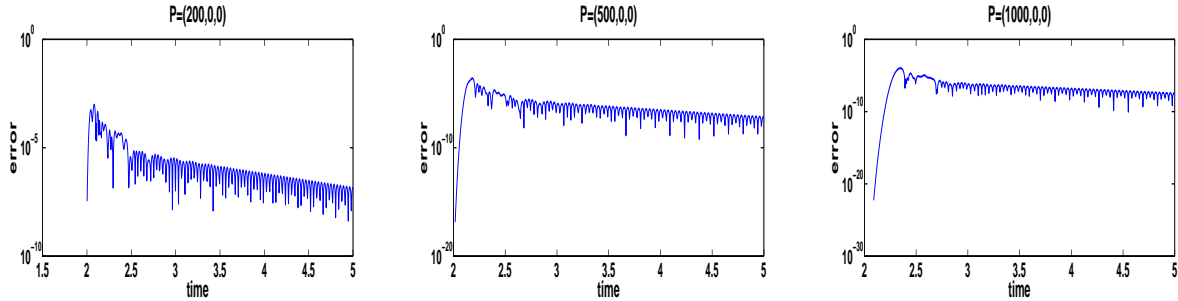


Figure 11: Example 3, case b). Absolute errors associated with  $u^S(P, t)$  for  $h_1$  at some  $P$ ,  $N = 1024$ ,  $N_0 = 41$ .



For what concerns the BEM-FEM approach, the artificial boundary  $\mathcal{B}$  is the sphere of radius 200 centered at the origin. In Figure 12 we show the solution  $u^{BF}$  obtained by partitioning the computational domain into  $n_T = 32368$  tetrahedra and  $n_{\Delta, \mathcal{B}} = 1772$  triangles, and time interval  $[0, 4]$  into  $N = 4096$  subintervals. The cutting integer, associated to  $\varepsilon = 1.0E - 05$ , is  $N_0 = 194$  ( $N_0^{est} = 226$ ). The finite element method has been associated with the (second order) Crank-Nicolson (C-N) time integrator.

This is a challenging numerical test because of the choice of  $f$ . Indeed, when the wave generated by the source  $f$  reaches the boundary  $\Gamma$ , the incompatibility between the homogeneous Dirichlet datum and the value of the impinging wave shows up through unacceptable oscillations in the numerical solution, caused by the time integrator we have associated to the FEM. We point out that the choice of a smaller threshold  $\varepsilon$  does not improve the behavior of

the solution. The oscillations are slightly reduced when the first order implicit Euler scheme is used, as Figure 13 shows.

Since the main purpose of this work is the use of the BIE (2) as a non reflecting boundary condition, we do not proceed further with the search of a proper time integrator to be associated with the FEM.

Figure 12: Example 3, case b). Solution  $u^{BF}(P, t)$  for  $h_1$  at some  $P$ ,  $N = 4096$ ,  $N_0 = 194$ . C-N time integrator.

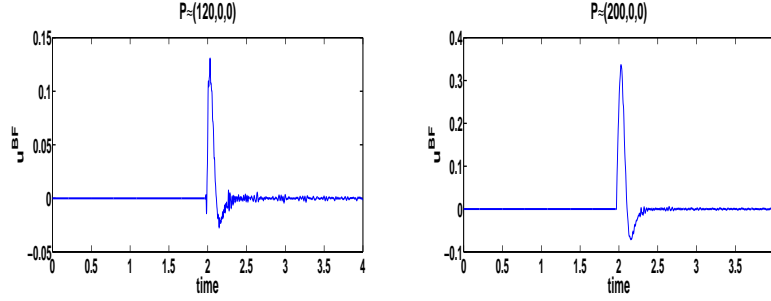


Figure 13: Example 3, case b). Solution  $u^{BF}(P, t)$  for  $h_1$  at some  $P$ ,  $N = 4096$ ,  $N_0 = 194$ . Implicit Euler time integrator.

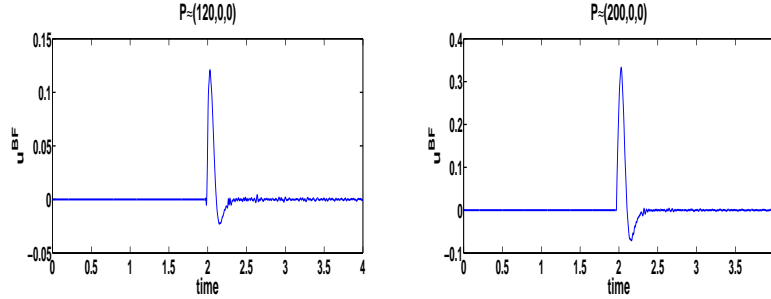
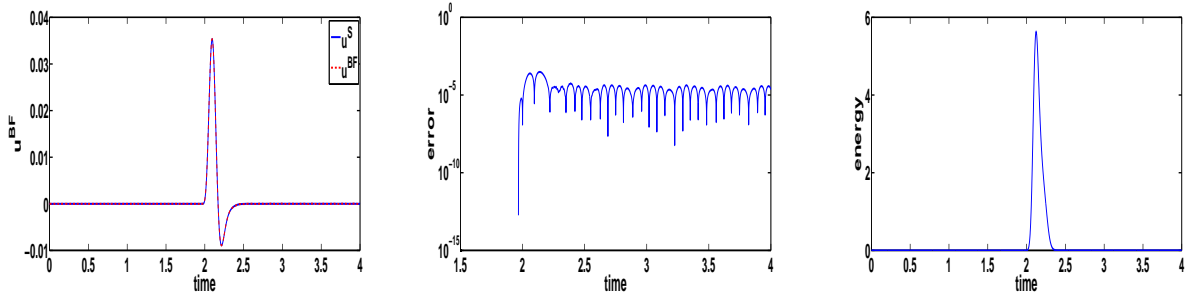


Figure 14: Example 3, case b). Solution  $u^{BF}(P, t)$  for  $h_2$  at  $P \approx (200, 0, 0)$  (left plot), associated absolute error (middle plot), and energy of the system (right plot),  $N = 4096$ ,  $N_0 = 194$ . C-N time integrator.



To confirm what we have remarked about the incompatibility of the chosen data, in Figure 14 we show that the oscillations disappear when, in the same setting considered above, in the

expression of  $f$ , instead of  $h_1$  we choose the following function  $h_2(t) = 10^7 t^3 e^{-(10t)^2} \sin(6t)$ . In this case too, the complete scheme could not run because of an out of memory.

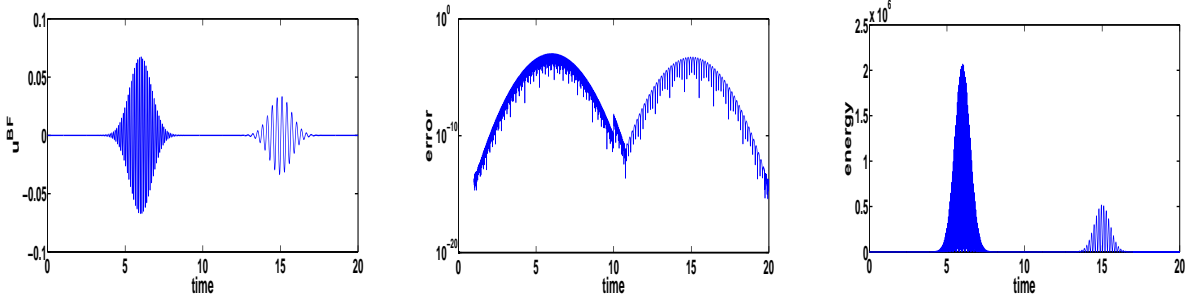
**Case c).** We conclude this example by considering a wave generated by two sources,

$$f_1(\mathbf{x}, t) = h_1(t) \delta(\mathbf{x} - \mathbf{x}_{0,1}), \quad \mathbf{x}_{0,1} = (6000, 0, 0), \quad h_1(t) = 10^4 e^{-(t-5)^2} \cos(60t),$$

$$f_2(\mathbf{x}, t) = h_2(t) \delta(\mathbf{x} - \mathbf{x}_{0,2}), \quad \mathbf{x}_{0,2} = (0, 60000, 0), \quad h_2(t) = 5 \cdot 10^4 e^{-(t-5)^2} \sin(20t).$$

The wave travels with velocity  $c = 6000$  towards the spherical obstacle of radius 1. The treatment of multiple sources, external to the finite computational domain, simply consists in the sum of the corresponding volume integrals. It is easy to check that in this case we have  $I_f = I_{f_1} + I_{f_2}$ , where  $I_{f_i}, i = 1, 2$  are given by (38).

Figure 15: Example 3, case c). Solution  $u^{BF}(P, t)$  at  $P \approx (2, 0, 0)$  (left plot), associated absolute error (middle plot), and energy of the system (right plot),  $N = 4096$ ,  $N_0 = 3$ .



In Figure 15, we show the behavior of the solution  $u^{BF}$  obtained by the BEM-FEM coupling at a point  $P \approx (2, 0, 0)$  in the time interval  $[0, 20]$ , the associated absolute error  $|u^S(P, t) - u^{BF}(P, t)|$ , and the energy of the system, in the computational domain bounded externally by the sphere of radius 2. The BEM reference solution  $u^S$  has been obtained by a discretization of the unit sphere into  $n_{\Delta, \Gamma} = 1770$  triangles. The solution  $u^{BF}$  has been computed by a decomposition of the shell into  $n_T = 32368$  tetrahedra; the triangular mesh inherited on the artificial boundary  $\mathcal{B}$  consists of  $n_{\Delta, \mathcal{B}} = 1772$  triangles. In both cases the time interval  $[0, 20]$  has been subdivided into  $N = 4096$  subintervals. The cutting strategy has been applied to the BEM-FEM with  $N_0 = 3$  ( $N_0^{est} = 6$ ), which corresponds to a threshold parameter  $\varepsilon = 1.0E - 05$ ; the complete scheme could not be performed because of an out of memory.

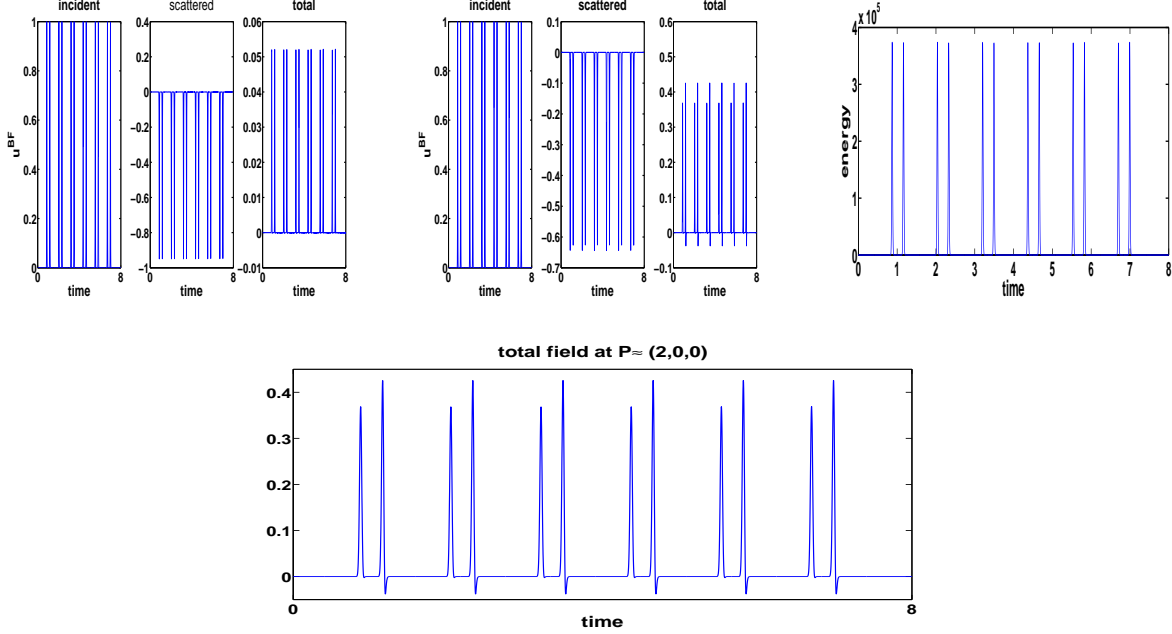
**Example 4.** As last test, we consider a plane wave impinging upon four scatterers, represented by spheres of radius 0.5 centered at the points  $C_1 = (1, 0, 0)$ ,  $C_2 = (-1, 0, 0)$ ,  $C_3 = (0, 1, 0)$  and  $C_4 = (0, -1, 0)$ . The velocity of propagation of the wave is  $c = 343$ . The incident wave  $u^{inc}$  consists of two wave packets, represented as the sum of six successive waves spaced at regular intervals along the  $x_1$ -axis, and the sum of six successive waves spaced at regular intervals along the  $x_2$ -axis. In particular,

$$u^{inc}(\mathbf{x}, t) = \sum_{i=1}^6 e^{-2 \cdot 10^{-2} (x_1 - \xi_i + ct)^2} + \sum_{i=1}^6 e^{-2 \cdot 10^{-2} (x_2 - \eta_i + ct)^2},$$

Figure 16: Example 4. The geometry of the problem: four spherical scatterers (left plot) and a section of the computational domain with a decomposition into tetrahedra (right plot).



Figure 17: Example 4. Incident, scattered and total field at  $P \approx (0,0,0)$  (top-left plot), at  $P \approx (2,0,0)$  (top-middle plot) and energy of the system (top-right plot). A zoom of the total field at  $P \approx (2,0,0)$  (bottom plot),  $N = 4096$ ,  $N_0 = 21$ .



with  $\xi_i=400,800,1200,1600,2000,2400$  and  $\eta_i=300,700,1100,1500,1900,2300$ . The solution is obtained by the BEM-FEM method, in the computational domain delimited by the surface of the sphere of radius 2 (see Figure 16). The time interval of interest  $[0, 8]$  has been subdivided into  $N = 4096$  subintervals. The domain has been discretized by  $n_T = 4122$  tetrahedra, and  $n_{\Delta,B} = 440$  triangles inherited on the artificial boundary. In spite of the high number of time instants we need to approximate accurately the picked behavior of the solution,  $N_0 = 21$  ( $N_0^{est} = 27$ ) matrices, corresponding to the threshold value  $\varepsilon = 1.0E - 05$ , are sufficient for the approximation of the NRBC without having any spurious reflection. In Figure 17 we show the behavior of the incident, the scattered and the total field at some points of the computational domain, as well as the energy of the system in the whole time interval  $[0, 8]$ . For this example, we can report the percentage of the ratios of the CPU times and of the

memory spaces: CPU-mat= 21% and CPU-rhs= 1%, while the ratio of the memory space is 0.5%.

## 5. Conclusions

In the last years, several papers have been published for the numerical solution of exterior problems for the classical wave equation, as testified by some of those reported in the bibliography. One of the main approaches is based on space-time boundary integral equation representations, which are either used to directly compute the problem solution, as in [15], [16] and [25] for example, or to define a non reflecting boundary condition to be coupled with a finite difference or finite element method, as in [13], [14] and [6]. A key issue for the success of the method is the computational cost and the required memory space of the associated discretization.

A good numerical approach, that has attracted the attention of several researchers, is based on Lubich discrete convolution quadratures (see [23]) coupled with classical Galerkin or collocation boundary element discretizations. To reduce its computational cost and memory space, several proposals have been made. All of them refer to the classical wave equation with unitary velocity, space domains whose sizes are of order one, and with small or very moderate time intervals. Furthermore, only the single-layer BIE representation is considered. The main goal of these proposals is the approximation of the full matrices generated by the Lubich formula, when this is coupled with a space Galerkin discretization, by corresponding sparse ones (see [20], [19], [5], [4]). However, the number of these matrices can be fairly large; this depends on the accuracy one wants to achieve and on the length of the time interval of integration.

In this paper we have considered a new class of problems, that often occur in practical applications, which allow to adopt a different and more effective strategy for the reduction of both the computational cost and the required working space. The space discretization is performed by a classical collocation BEM. For these problems, the above mentioned matrix sparsifications cannot be applied, as pointed out in Remark 3.2. Instead, we have shown that when the wave propagation velocity  $c$  is much larger than 1, the ratio between the physical domain size and the velocity  $c$  is small, and the problem transient is not excessively small, only the first  $N_0$  matrices, with  $N_0$  very small compared with their total number, are significant, and thus have to be constructed and stored. For the a priori choice of the integer  $N_0$  we have given a simple criterium. A consequence of this “truncation” is also the improvement of the stability of the solution method. To further improve the efficiency of Lubich’s formula, we have derived for its coefficients simple recurrence relationships, which allow their efficient evaluation.

All the numerical computation has been performed on a PC with Intel Core2<sup>®</sup> Quad Q6600 (2.40GHz). To perform our numerical testing we have written standard (i.e., sequential) Matlab<sup>®</sup> codes.

## References

- [1] M. Abramowitz, I. Stegun, Handbook of Mathematical Functions, National Bureau of Standards. A.M.S. 55, 1967.



- [2] A. Aimi, M. Diligenti, A. Frangi, C. Guardasoni, Energetic BEM-FEM coupling for wave propagation in 3D multidomains, *Internat. J. Numer. Methods Engrg.* 97 (2014) 377–394.
- [3] A. Aimi, M. Diligenti, C. Guardasoni, I. Mazzieri, S. Panizzi, An energy approach to space-time Galerkin BEM for wave propagation problems, *Internat. J. Numer. Methods Engrg.* 80 (2009) 1196–1240.
- [4] L. Banjai, M. Kachanovska, Fast convolution quadrature for the wave equation in three dimensions, *J. Comput. Phys.* 279 (2014) 103–126.
- [5] L. Banjai, M. Kachanovska, Sparsity of Runge-Kutta convolution weights for the three-dimensional wave equation, *BIT* 54 (4) (2014) 901–936.
- [6] L. Banjai, C. Lubich, F.-J. Sayas, Stable numerical coupling of exterior and interior problems for the wave equation, *Numer. Math.* 129 (2015) 611–646.
- [7] D. A. Bini, B. Meini, *Fast Reliable Algorithms for Matrices with Structure*, chap. Fast algorithms with applications to Markov chains and queueing models, SIAM, Philadelphia, PA, 1999, pp. 211–243.
- [8] D. Chappell, A convolution quadrature Galerkin boundary method for the exterior Neumann problem of the wave equation, *Math. Meth. Appl. Sci.* 32 (2009) 1585–1608.
- [9] P. J. Davies, D. B. Duncan, Stability and convergence of collocation schemes for retarded potential integral equations, *SIAM J. Numer. Anal.* 42 (3) (2004) 1167–1188.
- [10] P. J. Davies, D. B. Duncan, Convolution-in-time approximations of time domain boundary integral equations, *SIAM J. Sci. Comput* 35 (1) (2013) B43–B61.
- [11] D. A. Dunavant, High degree efficient symmetrical gaussian quadrature rules for the triangle, *Int. J. Num. Meth. Engng.* 21 (1985) 1129–1148.
- [12] S. Falletta, BEM coupling with the FEM-fictitious domain approach for the solution of the exterior Poisson problem and of the wave scattering by rotating rigid bodies, *IMA J. Num. Anal.*, doi: 10.1093/imanum/drw073, to appear.
- [13] S. Falletta, G. Monegato, An exact non reflecting boundary condition for 2D time-dependent wave equation problems, *Wave Motion* 51 (1) (2014) 168–192.
- [14] S. Falletta, G. Monegato, Exact non-reflecting boundary condition for 3D time-dependent multiple scattering-multiple source problems, *Wave Motion* 58 (2015) 281–302.
- [15] S. Falletta, G. Monegato, L. Scuderi, A space-time BIE methods for nonhomogeneous exterior wave equation problems. The Dirichlet case, *IMA J. Numer. Anal.* 32 (1) (2012) 202–226.

- [16] S. Falletta, G. Monegato, L. Scuderi, A space-time BIE method for wave equation problems: the (two-dimensional) Neumann case, *IMA J. Numer. Anal.* 34 (1) (2014) 390–434.
- [17] S. Falletta, S. Sauter, The panel-clustering method for the wave equation in two spatial dimensions, *J. Comput. Phys.* 305 (2016) 217–243.
- [18] S. Falletta, L. Scuderi, A new boundary element integration strategy for retarded potential boundary integral equations, *App. Num. Math.* 94 (2015) 106–126.
- [19] W. Hackbusch, W. Kress, S. Sauter, Sparse convolution quadrature for time domain boundary integral formulations of the wave equation, *IMA J. Numer. Anal.* 29 (2009) 158–179.
- [20] W. Kress, S. Sauter, Numerical treatment of retarded boundary integral equations by sparse panel clustering, *IMA J. Numer. Anal.* 1 (2008) 162–185.
- [21] A. Laliena, F.-J. Sayas, Theoretical aspects of the application of convolution quadrature to scattering of acoustic waves, *Numer. Math.* 112 (2009) 637–678.
- [22] S. Litynsky, Y. Muzychuk, A. Muzychuk, On the numerical solution of the initial-boundary value problem with Neumann condition for the wave equation by the use of Laguerre transform and boundary element method, *Acta Mechanica et Automatica* 10 (4) (2016) 285–290.
- [23] C. Lubich, Convolution quadrature and discretized operational calculus. I, *Numer. Math.* 52 (1988) 129–145.
- [24] C. Lubich, On the multistep time discretization of linear initial-boundary value problems and their boundary integral equations, *Numer. Math.* 67 (3) (1994) 365–389.
- [25] G. Monegato, L. Scuderi, A space-time BIE method for 2D mixed wave equation problems, *Appl. Math. Comp.* 259 (2015) 1046–1070.
- [26] G. Monegato, L. Scuderi, M. Stanić, Lubich convolution quadratures and their application to space-time BIEs, *Numerical Algorithms* 56 (3) (2011) 405–436.
- [27] S. Sauter, A. Veit, A Galerkin method for retarded boundary integral equations with smooth and compactly supported temporal basis functions, *Numer. Math.* 123 (1) (2013) 145–176.
- [28] F.-J. Sayas, *Retarded Potentials and Time Domain Boundary Integral Equations. A Road Map*, Springer Series in Computational Mathematics, Vol. 50, 2016.